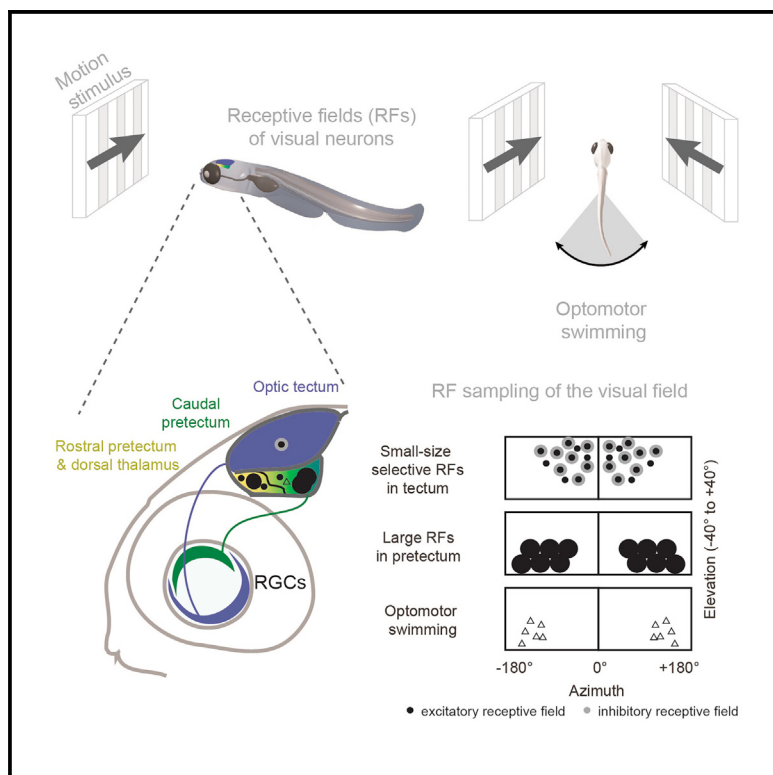


**Parallel Channels for Motion Feature Extraction in the Prepectum and Tectum of Larval Zebrafish****Graphical Abstract****Authors**

Kun Wang, Julian Hinz, Yue Zhang,  
Tod R. Thiele, Aristides B. Arrenberg

**Correspondence**

[aristides.arrenberg@uni-tuebingen.de](mailto:aristides.arrenberg@uni-tuebingen.de)

**In Brief**

Wang et al. show that the zebrafish optic tectum and pretectum extract visual motion features associated with hunting and optomotor behavior, respectively. The tectum preferably represents small stimuli in the upper nasal visual field, whereas the pretectum is biased toward larger stimuli in the lower visual field.

**Highlights**

- Optic tectum and pretectum sample visual space differently (upper nasal versus lower)
- Receptive fields are mainly small-size selective in tectum and large in pretectum
- Motion in the lower temporal visual field drives optomotor swimming
- The unequal sampling is likely an adaptation to hunting and optomotor behavior



# Parallel Channels for Motion Feature Extraction in the Prepectum and Tectum of Larval Zebrafish

Kun Wang,<sup>1,2,4</sup> Julian Hinz,<sup>1,2,4,5</sup> Yue Zhang,<sup>1,2</sup> Tod R. Thiele,<sup>3</sup> and Aristides B. Arrenberg<sup>1,6,\*</sup>

<sup>1</sup>Werner Reichardt Centre for Integrative Neuroscience, Institute for Neurobiology, University of Tübingen, 72076 Tübingen, Germany

<sup>2</sup>Graduate Training Centre for Neuroscience, University of Tübingen, 72074 Tübingen, Germany

<sup>3</sup>Department of Biological Sciences, University of Toronto Scarborough, Toronto, ON M1C 1A4, Canada

<sup>4</sup>These authors contributed equally

<sup>5</sup>Present address: Friedrich Miescher Institute for Biomedical Research, 4058 Basel, Switzerland

<sup>6</sup>Lead Contact

\*Correspondence: aristides.arrenberg@uni-tuebingen.de

<https://doi.org/10.1016/j.celrep.2019.12.031>

## SUMMARY

Non-cortical visual areas in vertebrate brains extract relevant stimulus features, such as motion, object size, and location, to support diverse behavioral tasks. The optic tectum and pretectum, two primary visual areas in zebrafish, are involved in motion processing, and yet their differential neural representation of behaviorally relevant visual features is unclear. Here, we characterize receptive fields (RFs) of motion-sensitive neurons in the diencephalon and midbrain. We show that RFs of many pretectal neurons are large and sample the lower visual field, whereas RFs of tectal neurons are mostly small-size selective and sample the upper nasal visual field more densely. Furthermore, optomotor swimming can reliably be evoked by presenting forward motion in the lower temporal visual field alone, matching the lower visual field bias of the pretectum. Thus, tectum and pretectum extract different visual features from distinct regions of visual space, which is likely a result of their adaptations to hunting and optomotor behavior, respectively.

## INTRODUCTION

Visual receptive fields (RFs) are specific regions in space where visual stimuli will alter the firing status of neurons (Spillmann, 2014). The ability of the visual system to extract useful information from the visual environment is directly related to the form, organization, and diversity of neuronal RFs within the vertebrate visual system. Task-relevant visual features are processed in parallel channels in the brain (Nassi and Callaway, 2009), starting in the retina (Baden et al., 2016).

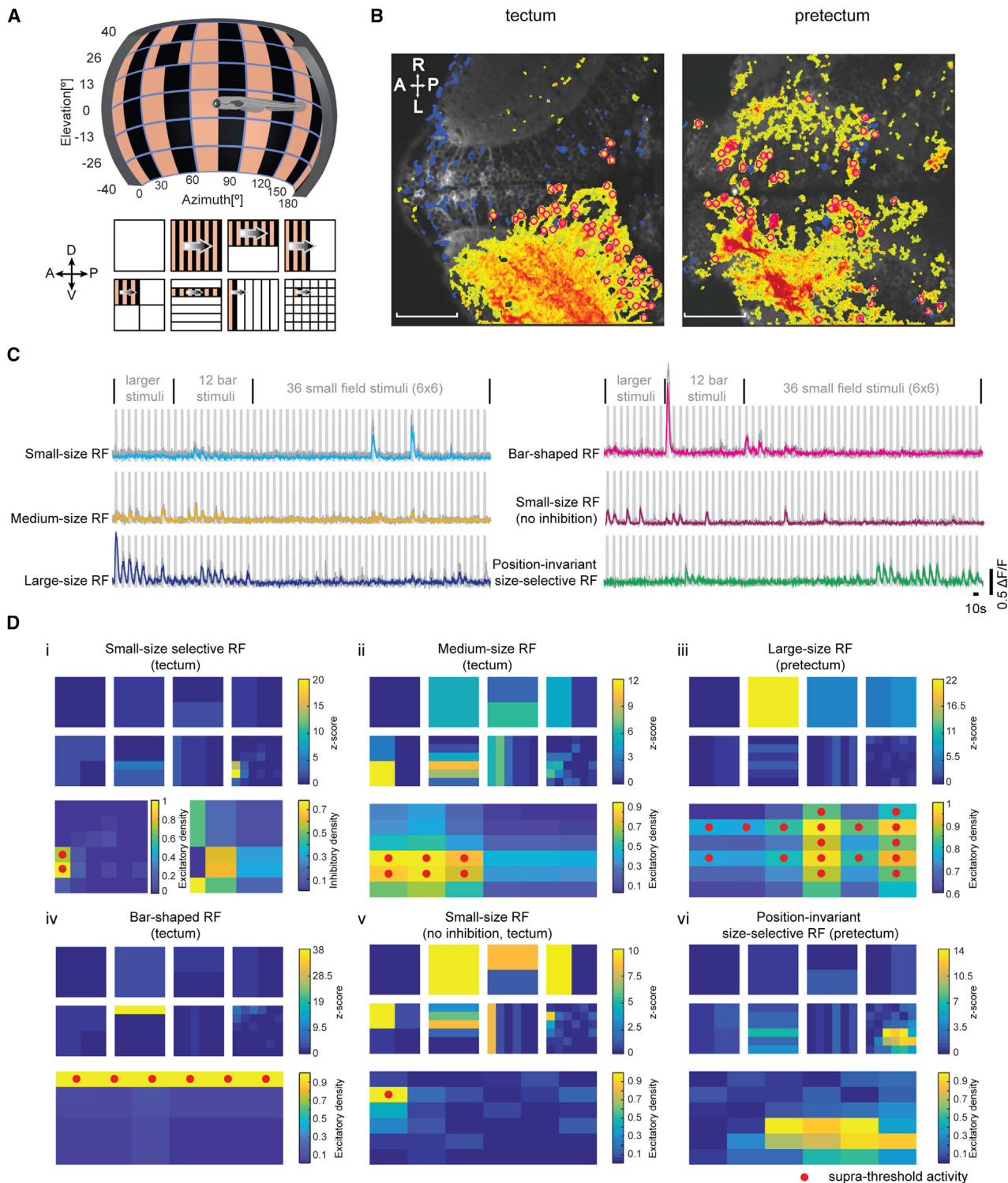
The optic tectum and pretectum, two brain regions in the mes- and diencephalon, receive direct input from direction-selective retinal ganglion cells (Giolli et al., 2006; Hunter et al., 2013; Robles et al., 2014) and encode visual stimuli moving in different directions (Wang et al., 2019). These evolutionarily ancient structures share developmental origins with the superior colliculus (tectum) and part of the accessory optic system (AOS) (pretec-

tum) in mammals. They support navigation and orienting behavior in zebrafish—which lack a visual cortex—already soon after hatching in 5-day-old larvae (Beck et al., 2004; Niell and Smith, 2005). Zebrafish are an important model organism for non-cortical vision research, but the division of feature extraction tasks between tectum and pretectum is still largely unknown. In particular, their roles in feature extraction in relation to behavioral tasks are crucial for a mechanistic understanding of sensorimotor transformations in zebrafish.

In the prepectal area and in the AOS of many vertebrates, neurons having large RFs with broad direction tuning curves are abundant (Britto et al., 1981; Grasse and Cynader, 1984; Massieck and Hoffmann, 2008; Simpson, 1984; Walley, 1967). Such large RFs should help the animal to distinguish wide-field optic flow from local motion and to estimate ego-motion. This computation is particularly important because many vertebrates use the outcome to stabilize gaze and body position (Portugues and Engert, 2009; Rinner et al., 2005). In larval zebrafish, both the optokinetic response (OKR) (Kubo et al., 2014) and the optomotor response (OMR) (Naumann et al., 2016) have been shown to rely on visual processing within the pretectum. In invertebrates, similar computations mediating OMR behavior were identified in the lobula plate, where horizontal system cells have large RFs with preferred directions matching the rotational optic flow around the yaw axis (Krapp et al., 2001). Additionally, it was shown that optogenetic manipulation of these neurons is sufficient to evoke yaw optomotor behaviors in fixed and tethered flies (Haikala et al., 2013; Busch et al., 2018). In zebrafish, the pretectum contains further anatomical sub-divisions (Yáñez et al., 2018), including structures involved in processing small visual stimuli during prey capture (Semmelhack et al., 2014; Muto et al., 2017), regions responsive to large-field motion stimuli (Kubo et al., 2014; Naumann et al., 2016), and a prepectal dopaminergic cluster providing input to the optic tectum (Tay et al., 2011). However, the RF properties of the pretectum at both the population and single neuron level are not known. It is also unclear how RF tuning within the pretectum may contribute to the production of visually mediated behaviors.

In contrast to the pretectum, RF sizes and locations for neurons within the zebrafish tectum have been described before (Niell and Smith, 2005; Sajovic and Levithal, 1982; Bergmann et al., 2018; Preuss et al., 2014; Zhang et al., 2011). Tectal neurons have relatively small RFs, conforming to the idea that tectal



**Figure 1.** Different Receptive Field (RF) Types Were Identified Using Horizontally Moving Gratings

(A) Stimuli of naso-temporally moving gratings covering view fields of variable sizes were presented to the animal's right eye ( $n = 8$  fish for naso-temporal and  $n = 2$  fish for temporal-nasal motion). Motion stimuli consisted of whole-field ( $1 \times 1$ ,  $180^\circ \times 80^\circ$ , azimuth  $\times$  elevation), half-field ( $2 \times 1/2$  and  $1/2 \times 2$ ), quarter-field ( $2 \times 2 \times 1/4$ ), bar ( $6 \times 1/6$  and  $1/6 \times 6$ ), and small-field ( $6 \times 6 \times 1/36$ , each  $30^\circ \times 13^\circ$ ) stimuli. The non-stimulated regions are shown in white for illustration purposes but contained a stationary grating. A snapshot during the small-field motion phase (depicted in the lower right) is shown on the display in the setup illustration (top).

(legend continued on next page)

neurons detect small-size moving objects in the view field and are needed for hunting behavior (Gahtan et al., 2005).

It is expected that each of the brain areas receiving input from the retina is adapted to the specific tasks and behaviors the animal executes in its environment. The behavioral relevance of a visual stimulus is influenced by the visual field location of the stimulus and will depend on the particular visually mediated behavior and the probability of observing such stimulus locations under natural conditions. For example, in the brain of macaque monkeys, it has been shown that RF properties in the superior colliculus, the homolog of the optic tectum, widely differ in the upper and lower visual view field, which likely represents adaptations to near space in the lower and far space in the upper visual field (Hafed and Chen, 2016). During hunting behavior, vertebrates typically keep the prey items, which are oftentimes small stimuli, in their nasal or frontal visual field, indicating that high visual acuity in this region of space is advantageous. Accordingly, both the primary visual cortex and superior colliculus show a magnification of foveal visual field regions (Grujic et al., 2018; Schwartz, 1980), i.e., more neurons are dedicated to representing these foveal locations than more peripheral locations. In the zebrafish retina, a region of heightened photoreceptor density (area centralis) has also been described (Schmitt and Dowling, 1999), corresponding to upper nasal visual field positions (Zimmermann et al., 2018). During prey capture, prey items need to be detected against the visual background, whereas for visual stabilization behaviors, animals need to detect their ego-motion by analyzing the global optic flow patterns resulting from the displacement of their bodies relative to the visual surround. To use brain resources efficiently, the reliable detection of optic flow directions is likely biased toward making use of the most informative visual field locations that occur in natural habitats and during behavior. The OMR is driven effectively by whole-field motion but—to our knowledge—there are no previous reports on particular visual field regions being preferably sampled by the animal to initiate OMR. Given the different roles of the optic tectum and the pretectum in hunting and stabilization behavior, respectively, it seems likely that these brain areas represent the visual field differently. It is unclear, however, whether the observed retinal anisotropies are relayed to primary visual areas in the zebrafish brain and whether magnifications of certain visual field locations exist in the tectum or pretectum of zebrafish. The characterization of such brain area-specific magnifications within the small vertebrate brain of larval zebrafish would advance our understanding of the efficient encoding of relevant information in the vertebrate brain

and help to reveal the specific computations that brains have evolved to perform.

Here, we characterize the RF properties of tectal and pretectal motion-sensitive neurons using *in vivo* 2-photon calcium imaging of GCaMP5G transgenic animals and investigate their organization in visual and anatomical space. In addition, we investigate how the identified RFs match to the visual locations, which drive the OMR behavior. Our results reveal complementary roles of the optic tectum and pretectum to support behaviorally relevant motion feature extraction.

## RESULTS

To estimate RF properties of pretectal and tectal neurons, we stimulated the right eye of immobilized larval zebrafish with a series of horizontally moving grating patterns of different sizes and locations (Figures 1A and S1; STAR Methods) and measured GCaMP5G calcium responses of neurons in the diencephalon and midbrain (Figure 1B). 1,926 motion-sensitive neurons that responded reliably during the three repetitions of the stimulus protocol were recorded in 10 animals. Neurons were divided into four functionally defined groups (Figures 1C, 1D, and S2; see STAR Methods for classification), based on the size and shape of their RFs: (1) small-size RFs, (2) medium-size RFs, (3) large-size RFs, and (4) bar-shaped RFs. RF sizes ranged from very small RFs ( $30^\circ \times 13^\circ$ ) to whole field ( $168^\circ$  azimuth  $\times 80^\circ$  elevation). In neurons with smaller RFs, we oftentimes observed suppressive effects for larger motion stimuli (Figure 1Di), showing that these neurons were small-size selective. Small-size RF neurons without signs of inhibition were frequently encountered as well; even though the excitatory RF density (STAR Methods) was localized to a small patch in the visual field, the neurons were also responsive to whole-field stimuli (Figure 1Dv). Furthermore, some of the small-size and medium-size RF neurons each responded to small moving stimuli in a range of different visual field positions but did not respond to larger moving stimuli covering the same visual field locations, i.e., their responses were small-size selective and position invariant (Figure 1Dvi).

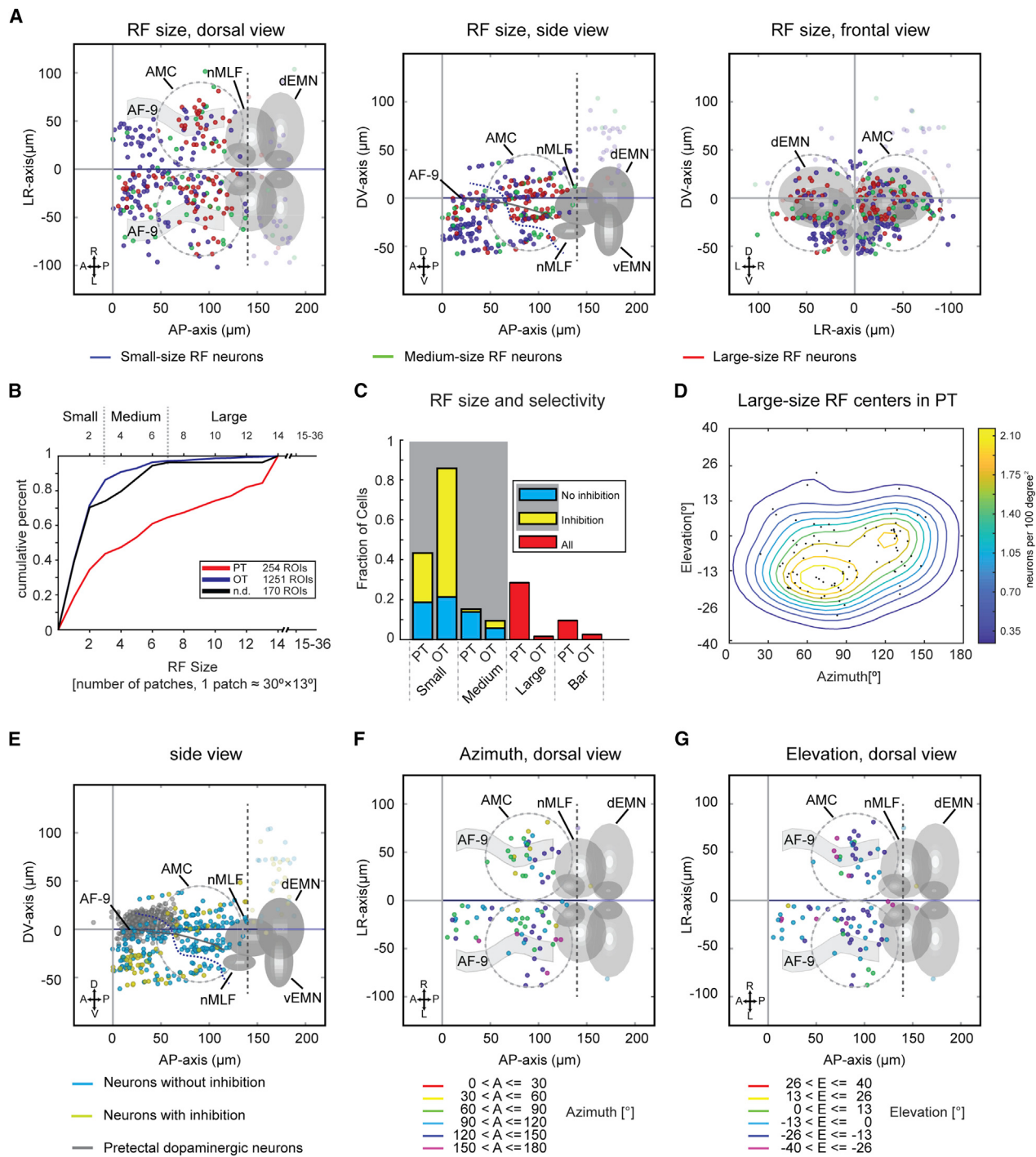
### Pretectal RFs Are Larger Than Tectal RFs and They Are Less Often Size Selective

For each motion-sensitive neuron, we measured the location of the RF center in the visual field and the anatomical position of the soma in the brain (see STAR Methods). Based on morphological tectal borders visible in our brain volumes and previous anatomical annotations of the pretectum and tegmentum

(B) The average fluorescence of an example calcium-imaging time series recorded from tectum and pretectum (PT) is shown in gray. Motion-sensitive image pixels are shown in false color, with warm and cold colors corresponding to positive and negative motion phase correlation, respectively. Manually selected regions of interest (ROIs) are labeled with magenta circles. Scale bar, 50  $\mu\text{m}$ ; A, anterior; P, posterior; L, left; R, right.

(C) Example  $\Delta F/F$  calcium responses of neurons with different RF sizes or shapes are shown. For each neuron, the colored trace corresponds to the median response across three repetitions (gray traces). The gray rectangular shades correspond to the 57 presented motion phases.

(D) RF maps for six example neurons corresponding to (C). Top: the eight squares correspond to the eight stimulus segments shown in (A), and each square corresponds to the stimulus arena surface ( $180^\circ \times 80^\circ$ , azimuth  $\times$  elevation). The calcium response is plotted as a Z score for each stimulus phase (for each ROI, the  $\Delta F/F$ , subtracted by the average of the  $\Delta F/F$ , divided by the standard deviation of the baseline  $\Delta F/F$ ). Bottom: by comparison of the activities evoked by spatially overlapping stimuli of different sizes, excitatory RF densities were calculated to measure the size of the RFs as the number of patches with supra-threshold activity (red dots). For cells with small-size excitatory RFs with maximal responses during the small-size stimulus phases (see STAR Methods), an inhibitory RF density was calculated to judge the extent of small-size selectivity (cell i). The anatomical location of each neuron is indicated (tectum or PT).

**Figure 2. Prepectal RFs Are Large and Biased toward the Lower Visual Field**

(A) Anatomical map of small-size (blue), medium-size (green), and large-size (red) RF neurons in the prepectal region. ( $n = 10$  fish, 5 composite prepectal regions). Each colored dot represents a single neuron. Coordinates are defined as distances relative to the posterior commissure in the diencephalon (anterior-posterior axis and dorso-ventral axis) and midline (left-right axis). Many identified neurons were located within the previously annotated main prepectal cluster (AMC, dashed circle; Kubo et al., 2014) and additional neurons were located further rostrally (in the rostral PT and in the dorsal thalamus; Figures S6A–S6D). Neurons located  $\geq 140 \mu\text{m}$  caudal to the posterior commissure (lighter colors) were located in the tegmentum and excluded from prepectal analysis (dashed gray line), whereas all rostral diencephalic neurons were included in the analysis.

(legend continued on next page)

(Kubo et al., 2014; Randlett et al., 2015), we identified tectal and tegmental neurons, as well as those located within the general pretectal area (Figure 2A). Neurons located in the tegmentum were excluded from further analysis. Within the general pretectal area, the caudal region corresponded to the pretectal anterior medial cluster (AMC) region described before (Kubo et al., 2014). In the recorded rostral diencephalic region, the dorsal part corresponded to the rostral pretectum (dorsal periventricular pretectal nucleus marked with dopaminergic neurons) and the ventral part to the dorsal thalamus annotated in the Z-Brain Atlas (Figures S6A–S6D) (Randlett et al., 2015; also see Discussion). However, the adult zebrafish brain contains several pretectal nuclei (Yáñez et al., 2018), and their exact identities and locations in the larval zebrafish brain still need to be resolved. We, therefore, included all diencephalic neurons in the analysis of the general pretectal area in this study. We investigated the topography of pretectal and tectal neurons as well as their sampling of the visual field. On average, we identified  $205 \pm 6$  motion-sensitive neurons per tectum and  $59 \pm 13$  neurons per pretectal region ( $n = 10$  fish, corresponding to 5 complete composite brains sampled in 10- $\mu\text{m}$  steps).

Pretectal neurons have larger excitatory RFs than those of tectal neurons (Figures 2B and 2C). Within the general pretectal area, 30% (88/295) of the motion-sensitive neurons had a large-size RF, compared to less than 2% (19/1,251) of the neurons within the tectum (Figure 2C). Most motion-sensitive tectal neurons (86%; Figure 2C) had excitatory RFs smaller than 1,200 deg<sup>2</sup> in area (3 of our small stimulus patches, each covering 30°  $\times$  13° in azimuth and elevation), which is consistent with previous reports from other groups (Sajovic and Levithal, 1982; Bergmann et al., 2018). Furthermore, similar to the findings in a previous report (Preuss et al., 2014), we found that 68% (853/1,251) of motion-sensitive neurons in the tectum were size selective, i.e., motion stimuli that were larger than the neuron's excitatory RF evoked lower calcium responses (Figures 1Di and 2C). In contrast, only 26% (77/295) of the motion-sensitive neurons in the general pretectal area were size selective (Figure 2C).

### Large-Size RFs in the Caudal Pretectum Are Biased to the Lower Visual Field

The RF centers of 69% of the large-size RF pretectal neurons were located in the lower visual field, which represents a significant bias (Figures 2D and S1B;  $p = 0.0002$ ,  $z$  test for one proportion).

These pretectal large-size RF neurons were located almost symmetrically in both hemispheres of the caudal pretectum, with some neurons in the rostral pretectum on the contralateral side (laterality index = -0.30; Figure 2A). The high number of ipsilateral neurons can—in part—be explained by reflections of the stimulus, which was revealed in an additional experiment in which the left eyes of the fish were blocked by a back foil (laterality index = -0.86;  $n = 6$  fish, 6 pretecta; Figure S1C). In addition to the large-size RF neurons observed in the caudal pretectum, many neurons responsive to small moving stimuli were also identified (Figures 1Cvi, 2A, S6E, and S6F). These small-size RF neurons were most frequent in the rostral diencephalic region, which corresponds to the rostral pretectum and the dorsal thalamus (see Discussion; Figures S6A–S6D).

Because functionally identified neurons in the rostral diencephalon segregated from those in the caudal pretectum through an anatomical gap containing only few motion-sensitive neurons (Figure 2A, side view), we defined a boundary based on this gap to separate these two anatomical clusters (dashed line in Figures 2A, S4A, and S4B, and STAR Methods). The rostral diencephalic region contained a higher proportion of small-size RFs (57%, 85/148) than the caudal pretectum (29%, 43/147;  $p < 0.001$ ,  $z$ -test for two proportions), whereas the caudal pretectum contained a higher proportion of large-size RFs (43%, 63/147) than the rostral diencephalic region (14%, 21/148;  $p < 0.001$ ,  $z$ -test for two proportions) (Figures 2A and S1C). Furthermore, the rostral region contained a higher proportion of small-size selective neurons (Figures 2E and S4B–S4D), whose activity was suppressed for larger stimuli (rostral region: 34% [51/148], caudal pretectum: 18% [26/147],  $n = 148$  and 147,  $p < 0.001$ ,  $z$ -test for two proportions, see STAR Methods). Rostral diencephalic neurons responsive to our smallest grating stimuli were also frequently (63% of the neurons,  $n = 6$  fish) responsive to small horizontally moving dots of variable diameters (3 to 18 degrees in diameter), as we tested in a separate experiment (data not shown).

It is well established that soma positions of zebrafish tectal neurons are topographically arranged within the tectum and that the RF centers cover almost the whole visual field at the population level (Attardi and Sperry, 1963; Niell and Smith, 2005; Romano et al., 2015; Bergmann et al., 2018). However, in the pretectum, we did not observe a clear topographic distribution of large-size RF neurons (Figures 2F, 2G, S1D, and S1E).

(B) Analysis of RF size differences across PT/diencephalon and optic tectum (OT). The cumulative distribution of RF sizes is shown for the general pretectal region within the diencephalon (PT, red), the OT (blue), and neurons of undefined provenance (black). Note that the PT has a larger fraction of large-size RF cells than the tectum.

(C) For each brain region (PT and OT), the fractions of small-size, medium-size, large-size, and bar-shaped RFs are shown. For small- and medium-size RFs, the inhibitory surround was investigated, and neurons with such inhibition are plotted in yellow.

(D) Locations and density contour plot of RF centers of large-size RF pretectal neurons in the contralateral and ipsilateral hemispheres ( $n = 10$  fish, 5 composite brains).

(E) Anatomical map of three types of neurons in the pretectal region: neurons with (yellow) and without (cyan) signs of inhibition and pretectal dopaminergic neurons (gray). The dopaminergic neurons served as a landmark for the dorsal periventricular pretectal nucleus in the rostral PT and were recorded in a separate experiment.

(F and G) Topographic maps of large-size RF neurons in the pretectal region. Each colored dot represents a single neuron with its RF center in the indicated azimuth (F) and elevation (G) range ( $n = 10$  fish, 5 composite pretectal regions).

Abbreviations are as follows: dEMN, dorsal extraocular motor neuron; vEMN, ventral extraocular motor neuron; dEMN and vEMN, the trochlear and oculomotor nuclei; nMLF, nucleus of the medial longitudinal fasciculus; A, anterior; P, posterior; D, dorsal; V, ventral; L, left; R, right; AF, arborization field. The abbreviations are applicable to all anatomical maps in this study.

### Tectal RFs Dominate the Upper Nasal View Field

As expected from the topographic retino-tectal projection of retinal ganglion cells, strong rostro-caudal, dorso-ventral, and medio-lateral topographical gradients of RF centers were found for small-size RF neurons in the optic tectum (Figures 3B, 3D, 3E, and S3A). Responding tectal neurons were mainly located in the contralateral hemisphere relative to the stimulated eye (laterality index = -0.88; Figures 3D and 3E; see STAR Methods). More tectal neurons with small-size RFs corresponding to the upper nasal visual field were found than corresponding to the lower temporal visual field (420 versus 55 neurons, upper nasal versus lower temporal view field, Z score test for proportions:  $p < 0.001$ ; Figures 3A and 3C). When comparing the upper nasal view field ( $26^\circ$  elevation,  $30^\circ$  azimuth) to the lateral view field ( $0^\circ$  elevation,  $90^\circ$  azimuth), the sampling difference corresponded to a 1.6-fold magnification factor (Figure S3B). In our experiments, we identified about 4 tectal small-size RF neurons per  $10^\circ \times 10^\circ$  in the upper nasal field in each completely sampled fish (hypothetical sampling every  $5\text{ }\mu\text{m}$  in the dorso-ventral direction, calculated based on our actually recorded 33.4 tectal motion-sensitive neurons per  $60^\circ \times 27^\circ$  in each of 5 composite brains sampled every  $10\text{ }\mu\text{m}$ ; see Figures S3B–S3D).

### Zebrafish OMR Behavior Is Driven Best by Motion in the Lower Temporal Visual Field

Although it is known that during hunting behavior, prey stimuli are mostly located in nasal visual field locations in zebrafish (Bianco et al., 2011), the visual field regions that drive OMR and OKR behavior have not been identified. OMR behavior can be stably induced with whole-field forward motion projected from below or from the side in larval zebrafish (Severi et al., 2014; Thiele et al., 2014), and it had been assumed that large—or even whole-field—stimuli are necessary to drive stabilization behaviors. Given the uneven distribution of large-size RFs in the upper and lower visual fields in the pretectum (Figure 2D), we wanted to test whether OMR is mainly driven by the forward motion located in the lower visual field, which would implicate the large-size RF neurons in mediating the OMR behavior. We, therefore, recorded the tail motion of larvae while forward-moving gratings of different sizes were presented in different visual field locations. Care was taken to always stimulate animals in a binocularly symmetric fashion to drive forward OMR instead of OMR turning behavior (Figures 4A, 4B, S5A, and S5B). The angle between the anterior-posterior body axis and the tail tip was traced to detect single tail beats and swim bouts (Figures 4A, 4D, and 4E). Bouts, consisting of a series of tail undulations beating symmetrically to both sides (forward OMR), were induced in response to whole-field forward-moving gratings (Video S1, S2, S3, and S4). In contrast, unsymmetrical unilateral turning swim beats to one side (turning OMR) were oftentimes evoked by whole-field rotating visual stimuli, although symmetrical beats (forward OMR) were also observed (Figure S5F). Whole-field and half-field visual stimuli covering the temporal or lower view field could evoke forward OMR robustly (Figure 4C).

To our surprise, forward OMR swim beats could be induced by stimuli as small as  $45^\circ \times 20^\circ$  (azimuth  $\times$  elevation, the smallest size in our protocol) in the lower temporal view field of both

eyes (Figure 4C). The OMR-evoking visual field locations were almost identical across all recorded animals ( $n = 6$ ; Figure 4F). To test whether the OMRs evoked by small stimuli are stronger than what would be expected under the assumption that OMR drive was established by the sum of equal-sized motion inputs across the visual field, we normalized the evoked OMR tail-beat rate to the respective stimulus field size (analogous to the excitatory RF density estimation; see STAR Methods). The resulting visual field map of OMR drive (Figure 4G) shows the disproportionately large influence of moving stimuli in the lower temporal view field. We then compared OMR drive across different stimulus sizes ( $1 \times 1$ ,  $2 \times 1$ , ...,  $4 \times 4$ ), always considering the visual field positions/stimulus phases that drove OMR best. This analysis revealed that the smallest stimulus area evoked responses, which were on average  $\sim 11$  times stronger than expected by an equal integration of optic flow inputs across the visual field (Figure 4H).

### DISCUSSION

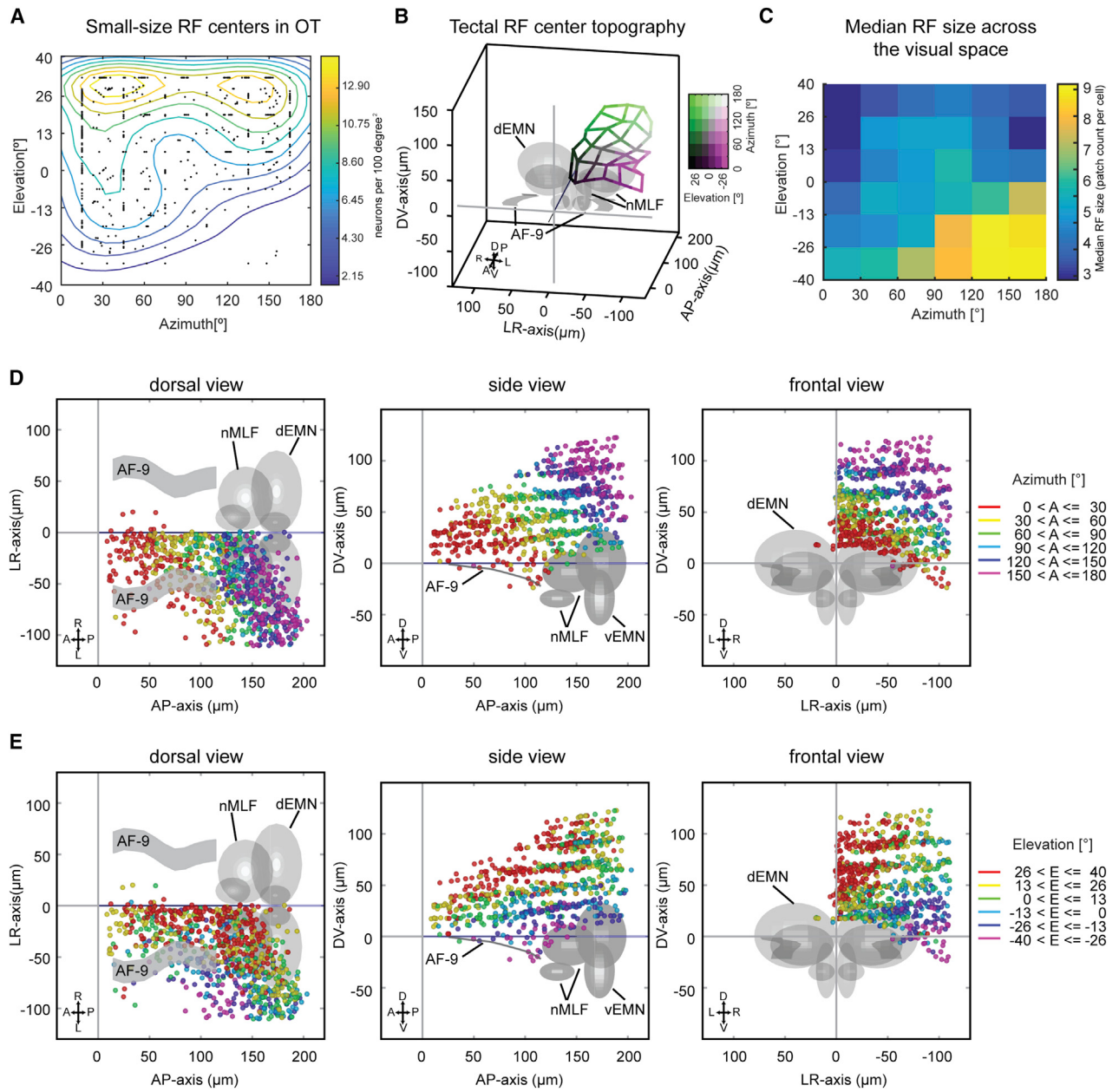
Our study reveals the functional segregation of visual motion processing in parallel channels, each extracting different sets of motion features across the visual field. The optic tectum, which processes the motion of small visual stimuli, has a bias for upper nasal visual field locations. Within the diencephalon, wide-field optic flow is mainly processed in the caudal pretectum using large RFs that mainly sample the lower visual field, whereas small motion stimuli are mainly processed in rostral regions of the diencephalon. Furthermore, we show that animals observe mainly the lower temporal visual field for optomotor forward swimming.

These findings agree with the need to process small visual stimuli, e.g., during prey capture (Preuss et al., 2014; Bianco et al., 2011), and the need to assess wide-field motion to inform stabilization behaviors (Kubo et al., 2014). The data support a circuit model in which these two distinct tasks are processed independently by multiple channels in different brain areas.

### Caudal and Rostral Diencephalic Regions Are Biased toward the Encoding of Large-Field Optic Flow and Small Stimuli, Respectively

Within the diencephalon, large-size RF neurons are mainly found in the caudal pretectal region, whereas small-size RF neurons are biased toward more rostral anatomical locations. The large-size RFs of pretectal neurons preferably sample the lower half of the visual field (Figures 2D and S1B), which fits with previous reports from pretectal neurons in dogfish (Masseck and Hoffmann, 2008). Due to our use of a half-cylindrical stimulus arena to present exclusively horizontally moving stimuli to the right eye, neurons with more complex, e.g., rotational, binocular, or vertical optic flow fields could not be described in this study (Kubo et al., 2014; Wang et al., 2019). These types of RF structures exist in visual neurons of other species (Krapp et al., 2001; Karmeier et al., 2003), and future studies are needed to identify them in zebrafish.

The adult zebrafish pretectum contains several nuclei distributed from the superficial to the periventricular regions, receives numerous retinal and tectal afferents, and projects to the optic

**Figure 3. Tectal RFs Are Small and Biased toward the Upper Nasal Visual Field**

(A) Visual field locations and density contour plot of RF centers of small-size RF tectal neurons ( $n = 10$  fish, 5 composite tecta).

(B) Anatomical map of the tectal RF center topography. The average anatomical position of neurons with their RF centers in each of the  $6 \times 6$  visual field bins was calculated and all 36 locations were connected by a grid to illustrate the mapping of visual space (color legend in the upper right) corresponding to anatomical space in the tectum (Figure S3A). The yaw angle ( $10^\circ$  right) and the pitch angle ( $20^\circ$  down) were adjusted to allow optimal view of the anatomical topography.

(C) Median RF size across the visual space. For each patch, we calculated the median RF sizes of all neurons (in tectum and PT) whose excitatory RFs covered the patch in question. The animals sample the lower temporal visual field mainly with large-size RF neurons, whereas small-size neurons dominate in the upper nasal visual field.

(D and E) Topographic maps of tectal small-size RF neurons for azimuth (D) and elevation (E). Each colored dot represents a single neuron with its RF center in the corresponding azimuth range in (D). For example, all RF centers of the neurons in red are located between  $0^\circ$  azimuth (in front of the fish) and  $30^\circ$  azimuth on the nasal right side of the fish. In (E), each colored dot represents a single neuron with its RF center in the corresponding elevation range. For example, RF centers of the neurons in green are located slightly above the equator of the view field ( $0^\circ$  to  $13^\circ$  in elevation).  $n = 10$  fish, 5 composite brains.

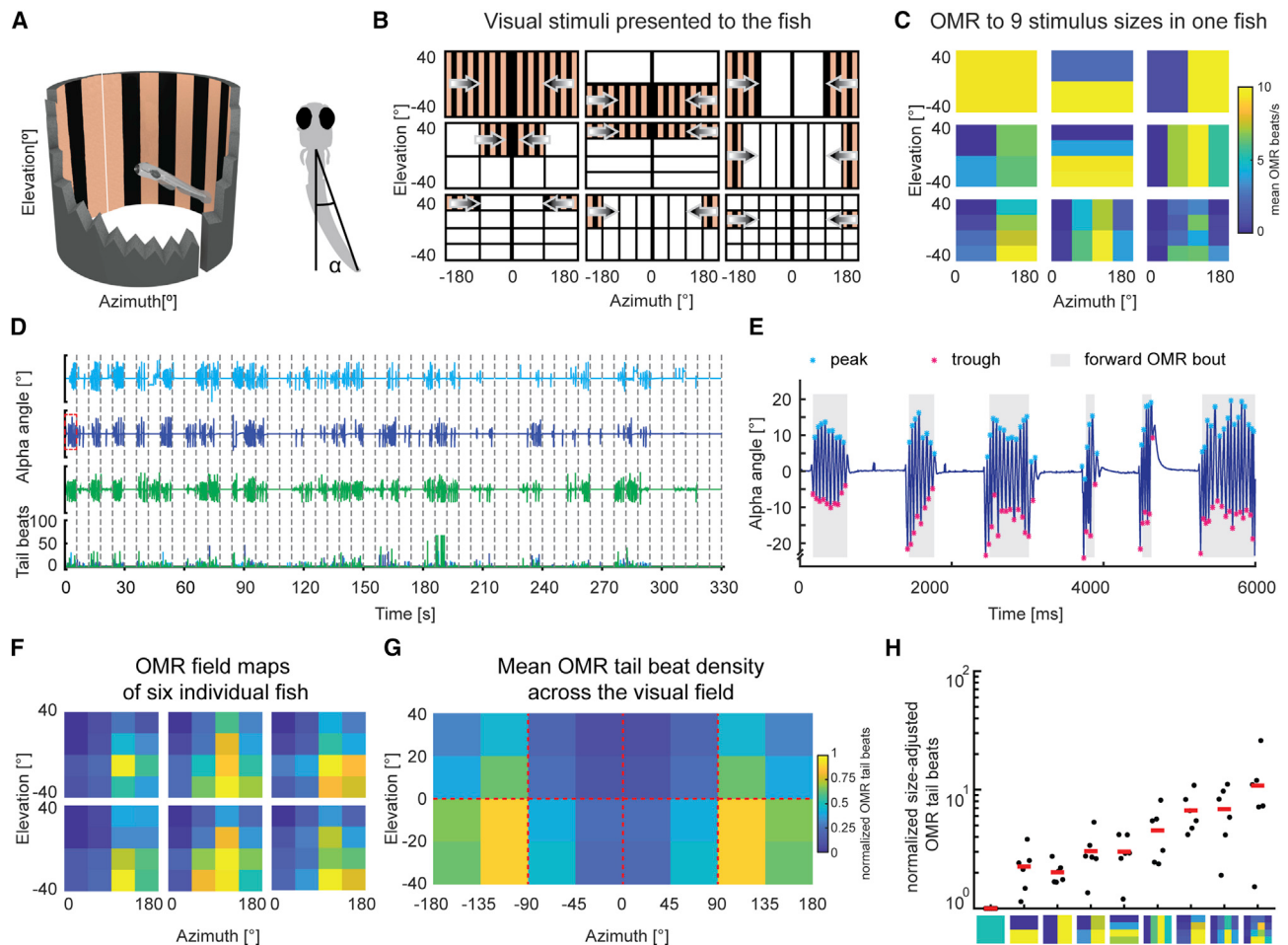


**Figure 4. Zebrafish Optomotor Responses Are Driven by Motion from Below and in the Rear of the Animal**

(A) Left: stimuli were presented binocularly to the animal with two half-cylindrical arenas while the behavior of the fish was recorded. A snapshot of the visual stimulus during the whole-field motion phase is shown in the setup illustration. Right: a schematic of a larval zebrafish performing OMR behavior. The indicated angle between the anterior-posterior body axis and the tail tip was measured to judge OMR performance.

(B) Motion stimuli of the OMR experiment consisted of whole-field ( $1 \times 1$ ,  $180^\circ$  azimuth  $\times 80^\circ$  elevation), half-field ( $2 \times 1/2$ ,  $1/2 \times 2$ ), quarter-field ( $2 \times 2 \times 1/4$ ), bar ( $4 \times 1/4$ ,  $1/4 \times 4$ ), medium-field ( $4 \times 2 \times 1/8$  and  $2 \times 4 \times 1/8$ ), and small-field ( $4 \times 4 \times 1/16$ , each  $45^\circ \times 20^\circ$ ) stimuli (for each size group, only one motion patch is illustrated). Each stimulus was mirror-symmetric about the mid-sagittal plane and shown with two half cylindrical arenas from both sides. The control stimulus phases (not shown in B) consisted of two stationary whole-field phases, counterclockwise and clockwise rotational moving gratings or looming visual stimuli on either side (Figure S5B). The regions in which no stimulus movement was present are shown as white areas for illustration purposes but contained a stationary grating.

(C) Average number of tail undulations per second for one larva, induced by forward-moving gratings of 9 different sizes (rectangles represent the stimulus hemifields from B).

(D) The full behavioral session for one animal, showing induced OMR behavior by stimuli of different sizes and locations as indicated in (B). The three stimulus repetitions are shown in different colors (cyan, blue, and green). Individual stimulus phases are separated by the dashed gray lines, and each row corresponds to 55 concatenated time periods in which motion stimuli were presented. The stimulus pauses in-between motion phases were cropped out and lasted 69 s each. Measured tail-beat counts (bottom) during each trial were consistent across the three repetitions.

(E) Tail movements induced by whole-field forward-moving gratings (from trial No. 2 indicated by a red rectangle in D). The peaks and troughs of each swim bout within the 6-s recording are labeled with cyan and magenta asterisks, respectively. OMR swim beats are indicated by gray background shade.

(F) Visual field heatmaps of the forward-OMR tail-beat rate for six individual larval zebrafish ( $n = 6$ ). The visual field density of OMR behavior was quantified analogous to the excitatory RF densities in Figure 1. The density was normalized according to the size of the stimulation area in each fish individually (see STAR Methods).

(G) Average heatmap of the OMR beat density for stimulation across different visual field coordinates ( $n = 6$  fish).

(H) Maximum OMR beats for each of the 9 stimulus fields shown in (B) and (C) after normalization according to stimulus size (see STAR Methods).

tectum as well (Fernald and Shelton, 1985; Presson et al., 1985; Kastenhuber et al., 2010; Yáñez et al., 2018). The correspondence of these nuclei to functionally defined larval brain regions

is not fully resolved (Kubo et al., 2014; Muto et al., 2017; Semmelhack et al., 2014; Arrenberg and Driever, 2013). In our study, the pretectal dopaminergic neurons, which are evolutionarily

conserved across most amniotes (Yamamoto and Vernier, 2011), were used as a landmark to indicate the location of the periventricular pretectal nucleus (Filippi et al., 2014). The location of caudal pretectal neurons in this study corresponds to the AMC, previously described by Kubo et al. (2014), as well as to the annotated pretectal brain volume in the Z-Brain Atlas (Figures S6A–S6C; Randlett et al., 2015). Recorded extra-tectal neurons located more than 140  $\mu\text{m}$  caudal to the posterior commissure most likely belonged to the tegmentum and were, therefore, excluded from the pretectal analysis (see STAR Methods). The rostral diencephalic neurons described in this study cover rostral pretectal and dorsal thalamic brain regions (Videos S5, S6, and S7) (Rupp et al., 1996; Yáñez et al., 2018). Functional properties of two larval pretectal nuclei have previously been described in relation to prey capture (parvocellular and magnocellular superficial nuclei [PSP and PSM]); however, they are located more laterally than the bulk of our recorded motion-sensitive neurons in the rostral pretectum (Semmelhack et al., 2014; Muto et al., 2017). Morphologically, the identity, extent, and overlap of larval pretectal neuron populations, which give rise to each of the known adult pretectal nuclei, is not easily discernible (Arrenberg and Driever, 2013). Further anatomical studies are needed to link our functionally identified neurons to specific pretectal and thalamic brain nuclei and connectivity in the larval brain.

The anatomical and visual field locations, as well as neuron numbers, were consistent for large-size RF neurons in the pretectum across fish and experiments (Figures 2A, 2D, S1B, and S1C), whereas the responses of position-invariant RF neurons (Figure 1Dvi) appeared to be more variable. Notably, the preferred visual field locations, exact anatomical locations, and the number of identified position-invariant neurons within the diencephalon differed in the first and second experiment we performed (Figures S4E and S4F). Further work is needed to elucidate the specific anatomical distribution and response properties of position-invariant RF neurons.

#### The Tectum—Poised for Prey Capture

Our analysis of a large number of tectal neurons extends previous reports on tectal physiology (Niell and Smith, 2005; Sajovic and Levinthal, 1982; Zhang et al., 2011; Preuss et al., 2014). Our finding that the tectum mostly comprises relatively small excitatory RFs, which oftentimes are small-size selective, is in agreement with a role of the tectum in prey capture (Bianco et al., 2011; Gahtan et al., 2005). It is noteworthy that our stimulus protocol only allowed the measurement of RF sizes down to 30° horizontally and 13° vertically (corresponding to our smallest visual stimulus), which is much larger than the minimal RF size in a previous report (Preuss et al., 2014). Also, due to the limitation of 2-photon calcium imaging, we are not able to directly assess inhibition but assess it only indirectly by comparing the reduction in responses evoked by larger stimuli.

The topographic arrangement of the zebrafish tectal neurons is well established both for the anatomical retino-tectal projection (Baier et al., 1996; Trowe et al., 1996) and the functional RF mapping (Bergmann et al., 2018; Niell and Smith, 2005). However, precise measurements of dedicated tectal anatomical volumes had not been performed previously and are needed to build faith-

ful models of zebrafish vision. We find that the upper nasal visual field ( $134 \mu\text{m}^3/\text{deg}^2$ ) is magnified in the tectum by a factor of 1.6 relative to lateral ( $82 \mu\text{m}^3/\text{deg}^2$ ) visual field locations (Figure S3), which is a relatively mild magnification in comparison to foveal magnification in the primate superior colliculus and visual cortex (Schwartz, 1980; Cowey and Rolls, 1974; Grujic et al., 2018). Given that the larval prey capture behavior depends on the optic tectum and larvae respond to the paramecia located in front and extending 60° temporalward of the fish (Bianco et al., 2011; Romano et al., 2015), a role of these tectal small-size RF neurons in prey capture seems likely. Because the density of small-size RF neurons is elevated in the upper nasal view field (Figures 3A and S3B), this would suggest that larval prey capture performance is best when the paramecia are located in front and slightly above the eyes and possibly the mouth. In this study, we have only investigated the RF distributions at a single developmental stage. It is possible that the reported tectal magnification of the upper nasal visual field is (in part) a result of the tectal developmental stage because new, initially non-functional neurons are added in the dorso-medial and caudo-lateral tectum (Boulanger-Weill et al., 2017; Recher et al., 2013).

#### The OMR Is Driven Most Strongly by the Lower Temporal Visual Field

Although it had been known from previous reports that motion stimuli presented from the bottom or from the side are effective in triggering OMR behavior (Thiele et al., 2014; Severi et al., 2014; Orger et al., 2008), it was unclear which parts of the visual field the animal preferentially responds to. We tested motion stimuli of variable size and position against a stationary background and show that for forward swimming OMR, the relevant region lies in the lower temporal view field of the fish (Figures 4F and 4G). We found that even motion stimuli as small as  $45^\circ \times 20^\circ$  (azimuth  $\times$  elevation) can be effective OMR stimuli. This finding is in contrast to the concept that the OMR is a whole-field-induced behavior. Rather, it suggests that distinct parts of the visual field are sampled for body stabilization behaviors. This most likely reflects the ecological adaptions of zebrafish living in shallow waters (Engeszer et al., 2007) and the need to sample the most relevant parts of the visual field for different tasks (Zimmermann et al., 2018), such as putative high contrast textures within a river bed. Notably, zebrafish also sample different parts of their visual field for a related stabilization behavior, the OKR. The OKR of zebrafish is best driven by stimuli located laterally and slightly elevated (Dehmelt et al., 2019). Thus, each visually mediated behavior that has been investigated for visual field anisotropies (OMR, OKR, and prey capture behavior) preferentially samples information from different parts of visual space.

Because RGCs project directly to the optic tectum and pretectum (Robles et al., 2014), it seems likely that the small-size RFs without inhibition as well as the large-size RFs in the caudal pretectum are established by direct inputs from RGCs (Figure 5). Small-size-selective responses require inhibitory inputs, which could be calculated already within the retina or within the retino-recipient brain areas (Grama and Engert, 2012; Ramdy and Engert, 2008).

Previous work suggests that visual stabilization behaviors are driven by the caudal pretectum (Naumann et al., 2016; Wang

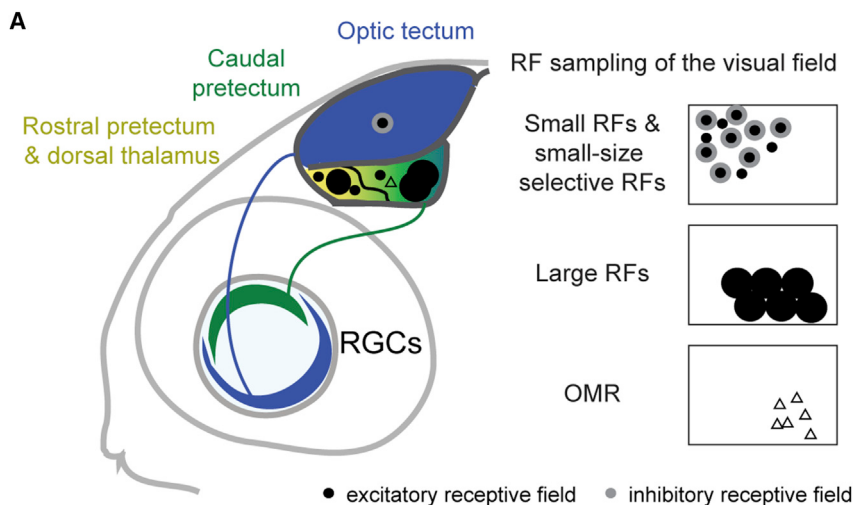


**Figure 5. Illustration of the Major Anatomical Locations and Visual Field Preferences of the Characterized Functional Cell Types**

The tectum mainly contains small-size-selective RFs, whereas a distribution of different RFs is observed in the PT and dorsal thalamus, ranging from small-size-selective (mainly in the rostral PT and dorsal thalamus) to large-size RFs (mainly in the caudal PT). Previous findings suggest that tectum and caudal PT receive direct retinal inputs (solid lines). To the right, the visual field distributions of RF centers are shown for each functional cell type. An additional visual field map is shown for OMR behavior, in which the regions driving OMR best are indicated. In the visual field maps, the horizontal axis (left-right) corresponds to the nasal-temporal spatial locations and the vertical axis to the upper and lower visual field locations.

et al., 2019; Kubo et al., 2014), which we show contains neurons of different RF sizes. Both whole-field and small-size optic flow stimuli evoke robust OMR tail beats, suggesting that both pre-tectal large-size and small-size RF neurons might form the basis for optic flow processing underlying the OMR. In agreement with this possibility, the RF centers of both pre-tectal large-size and small-size RFs match the bias of OMR drive to lower visual field locations (Figures S5E, S6E, and S6F). Further work is needed to identify the relative contributions of large-size RF and small-size RF pre-tectal neurons to OMR behavior.

In summary, we mapped the RFs of zebrafish tectal and pre-tectal neurons and demonstrated that both brain areas fulfill complementary roles for visual motion feature extraction. RFs of tectal neurons are predominantly small and size selective and have a strong bias in representing the upper nasal visual field (Figure 5). In contrast, caudal pre-tectal neurons have predominantly larger RFs with RF centers preferentially located in the lower visual field of the animal, which corresponds to the location of strongest OMR drive in the lower temporal visual field. Thus, each tectal and pre-tectal brain region extracts different motion stimulus features and samples distinct visual field regions. We speculate that this anisotropic visual field sampling in the tectum and pre-tectum could represent adaptations of zebrafish to feeding and stabilization behaviors, resulting in efficient usage of visual brain area volumes for the representation of behaviorally relevant stimulus features. Our study reveals the sensory layout of motion processing and, thus, constitutes an important advance for deriving a biologically faithful model of visuomotor transformations in zebrafish.

## STAR★METHODS

Detailed methods are provided in the online version of this paper and include the following:

- KEY RESOURCES TABLE
- LEAD CONTACT AND MATERIALS AVAILABILITY

## ● EXPERIMENTAL MODEL AND SUBJECT DETAILS

- Animal care and transgenic lines

## ● METHOD DETAILS

- Animal preparation (tectal and pre-tectal imaging of neuronal somata)
- 2-photon microscopy of somatic calcium responses
- LED arena for visual stimulation (Figures 1, 2, 3, and 4)
- Identification of regions of interest (imaging of neuronal somata)
- Defining the borders of the tectum in our 3D datasets
- Registration of 3D pre-tectal volume from Z Brain atlas (related to Figure S6)
- Movies of 3D brain volumes with neurons shown inside
- Monocular receptive field mapping
- Inclusion criteria for somatic calcium responses
- Setup for measuring the receptive field of OMR behavior
- Receptive field mapping of OMR behavior

## ● QUANTIFICATION AND STATISTICAL ANALYSIS

## ● DATA AND CODE AVAILABILITY

## SUPPLEMENTAL INFORMATION

Supplemental Information can be found online at <https://doi.org/10.1016/j.celrep.2019.12.031>.

## ACKNOWLEDGMENTS

We thank Väinö Haikala and Dierk F. Reiff for help with the visual stimulus arena. The identification of the anatomical position of pre-tectal dopaminergic neurons was conducted in collaboration with Wolfgang Driever and Christian Altbürguer, who provided anatomical z stacks of a double-transgenic dopaminergic line (unpublished data; see Fernandes et al., 2012 and Reinig et al., 2017). Furthermore, we thank Thomas Nieß (glassblower shop, University of Tübingen) and Klaus Vollmer (fine mechanics workshop, University Clinic Tübingen) for technical support, Prudenter-Agas (Hamburg, Germany) for generating illustrations, and Julianne Skinner for contributing to the analysis of RF center distribution. We thank Martin Meyer for feedback on a previous version of the manuscript. This work was funded by Deutsche Forschungsgemeinschaft (DFG) grants EXC307 (CIN-Werner Reichardt Centre

for Integrative Neuroscience) and INST 37/967-1 FUGG and Human Frontier Science Program (HFSP) Young Investigator grant RGY0079.

## AUTHOR CONTRIBUTIONS

K.W. performed the experiments on pretectal and tectal somatic responses. K.W., J.H., and Y.Z. analyzed the data. A.B.A., K.W., J.H., and T.R.T. conceived the experiments and associated analysis protocols. K.W., J.H., and A.B.A. wrote the manuscript, with input from T.R.T.

## DECLARATION OF INTERESTS

The authors declare no competing interests.

Received: May 17, 2019

Revised: July 27, 2019

Accepted: December 9, 2019

Published: January 14, 2020

## REFERENCES

- Ahrens, M.B., Huang, K.H., Narayan, S., Mensh, B.D., and Engert, F. (2013a). Two-photon calcium imaging during fictive navigation in virtual environments. *Front. Neural Circuits* 7, 104.
- Ahrens, M.B., Orger, M.B., Robson, D.N., Li, J.M., and Keller, P.J. (2013b). Whole-brain functional imaging at cellular resolution using light-sheet microscopy. *Nat. Methods* 10, 413–420.
- Arrenberg, A.B., and Driever, W. (2013). Integrating anatomy and function for zebrafish circuit analysis. *Front. Neural Circuits* 7, 74.
- Attardi, D.G., and Sperry, R.W. (1963). Preferential selection of central pathways by regenerating optic fibers. *Exp. Neurol.* 7, 46–64.
- Baden, T., Berens, P., Franke, K., Román Rosón, M., Bethge, M., and Euler, T. (2016). The functional diversity of retinal ganglion cells in the mouse. *Nature* 529, 345–350.
- Baier, H., Klostermann, S., Trowe, T., Karlstrom, R.O., Nüsslein-Volhard, C., and Bonhoeffer, F. (1996). Genetic dissection of the retinotectal projection. *Development* 123, 415–425.
- Beck, J.C., Gilland, E., Tank, D.W., and Baker, R. (2004). Quantifying the ontogeny of optokinetic and vestibuloocular behaviors in zebrafish, medaka, and goldfish. *J. Neurophysiol.* 92, 3546–3561.
- Bergmann, K., Meza Santoscoy, P., Lygdaas, K., Nikolaeva, Y., MacDonald, R.B., Cunliffe, V.T., and Nikolaev, A. (2018). Imaging Neuronal Activity in the Optic Tectum of Late Stage Larval Zebrafish. *J. Dev. Biol.* 6, E6.
- Bianco, I.H., Kampff, A.R., and Engert, F. (2011). Prey capture behavior evoked by simple visual stimuli in larval zebrafish. *Front. Syst. Neurosci.* 5, 101.
- Boulanger-Weill, J., Candat, V., Jouary, A., Romano, S.A., Perez-Schuster, V., and Sembre, G. (2017). Functional Interactions between Newborn and Mature Neurons Leading to Integration into Established Neuronal Circuits. *Curr. Biol.* 27, 1707–1720.e5.
- Britto, L.R., Natal, C.L., and Marcondes, A.M. (1981). The accessory optic system in pigeons: receptive field properties of identified neurons. *Brain Res.* 206, 149–154.
- Busch, C., Borst, A., and Mauss, A.S. (2018). Bi-directional Control of Walking Behavior by Horizontal Optic Flow Sensors. *Curr. Biol.* 28, 4037–4045.e5.
- Chen, T.W., Wardill, T.J., Sun, Y., Pulver, S.R., Renninger, S.L., Baohan, A., Schreiter, E.R., Kerr, R.A., Orger, M.B., Jayaraman, V., et al. (2013). Ultrasensitive fluorescent proteins for imaging neuronal activity. *Nature* 499, 295–300.
- Cowey, A., and Rolls, E.T. (1974). Human cortical magnification factor and its relation to visual acuity. *Exp. Brain Res.* 21, 447–454.
- Dehmelt, F.A., Meier, R., Hinz, J., Yoshimatsu, T., Simacek, C.A., Wang, K., Baden, T., and Arrenberg, A.B. (2019). Spherical arena reveals optokinetic response tuning to stimulus location, size and frequency across entire visual field of larval zebrafish. *bioRxiv*. <https://doi.org/10.1101/754408>.
- Engeszer, R.E., Patterson, L.B., Rao, A.A., and Parichy, D.M. (2007). Zebrafish in the wild: a review of natural history and new notes from the field. *Zebrafish* 4, 21–40.
- Euler, T., Susanne, H., E., Margolis, D., J., Breuninger, T., Castell, X., Detwiler, P., B., and Denk, W. (2009). Eyecup scope—optical recordings of light stimulus-evoked fluorescence signals in the retina. *Pflügers Archiv - European Journal of Physiology* 457, 1393–1414.
- Fernald, R.D., and Shelton, L.C. (1985). The organization of the diencephalon and the pretectum in the cichlid fish, *Haplochromis burtoni*. *J. Comp. Neurol.* 238, 202–217.
- Fernandes, A.M., Fero, K., Arrenberg, A.B., Bergeron, S.A., Driever, W., and Burgess, H.A. (2012). Deep brain photoreceptors control light-seeking behavior in zebrafish larvae. *Curr. Biol.* 22, 2042–2047.
- Filippi, A., Mueller, T., and Driever, W. (2014). vglut2 and gad expression reveal distinct patterns of dual GABAergic versus glutamatergic cotransmitter phenotypes of dopaminergic and noradrenergic neurons in the zebrafish brain. *J. Comp. Neurol.* 522, 2019–2037.
- Gahtan, E., Tanger, P., and Baier, H. (2005). Visual prey capture in larval zebrafish is controlled by identified reticulospinal neurons downstream of the tectum. *J. Neurosci.* 25, 9294–9303.
- Giolli, R.A., Blanks, R.H., and Lui, F. (2006). The accessory optic system: basic organization with an update on connectivity, neurochemistry, and function. *Prog. Brain Res.* 151, 407–440.
- Grama, A., and Engert, F. (2012). Direction selectivity in the larval zebrafish tectum is mediated by asymmetric inhibition. *Front. Neural Circuits* 6, 59.
- Grasse, K.L., and Cynader, M.S. (1984). Electrophysiology of lateral and dorsal terminal nuclei of the cat accessory optic system. *J. Neurophysiol.* 51, 276–293.
- Grujic, N., Brehm, N., Gloge, C., Zhuo, W., and Hafed, Z.M. (2018). Perisaccadic perceptual mislocalization is different for upward saccades. *J. Neurophysiol.* 120, 3198–3216.
- Hafed, Z.M., and Chen, C.Y. (2016). Sharper, Stronger, Faster Upper Visual Field Representation in Primate Superior Colliculus. *Curr. Biol.* 26, 1647–1658.
- Haikala, V., Joesch, M., Borst, A., and Mauss, A.S. (2013). Optogenetic control of fly optomotor responses. *J. Neurosci.* 33, 13927–13934.
- Hunter, P.R., Lowe, A.S., Thompson, I.D., and Meyer, M.P. (2013). Emergent properties of the optic tectum revealed by population analysis of direction and orientation selectivity. *J. Neurosci.* 33, 13940–13945.
- Joesch, M., Plett, J., Borst, A., and Reiff, D.F. (2008). Response properties of motion-sensitive visual interneurons in the lobula plate of *Drosophila melanogaster*. *Curr. Biol.* 18, 368–374.
- Karmeier, K., Krapp, H.G., and Egelhaaf, M. (2003). Robustness of the tuning of fly visual interneurons to rotatory optic flow. *J. Neurophysiol.* 90, 1626–1634.
- Kastenhuber, E., Kratochwil, C.F., Ryu, S., Schweitzer, J., and Driever, W. (2010). Genetic dissection of dopaminergic and noradrenergic contributions to catecholaminergic tracts in early larval zebrafish. *J. Comp. Neurol.* 518, 439–458.
- Krapp, H.G., Hengstenberg, R., and Egelhaaf, M. (2001). Binocular contributions to optic flow processing in the fly visual system. *J. Neurophysiol.* 85, 724–734.
- Kubo, F., Hablitzel, B., Dal Maschio, M., Driever, W., Baier, H., and Arrenberg, A.B. (2014). Functional architecture of an optic flow-responsive area that drives horizontal eye movements in zebrafish. *Neuron* 81, 1344–1359.
- Marques, J.C., Lackner, S., Felix, R., and Orger, M.B. (2018). Structure of the Zebrafish Locomotor Repertoire Revealed with Unsupervised Behavioral Clustering. *Curr. Biol.* 28, 181–195.e5.
- Masseck, O.A., and Hoffmann, K.P. (2008). Responses to moving visual stimuli in pretectal neurons of the small-spotted dogfish (*Scyliorhinus canicula*). *J. Neurophysiol.* 99, 200–207.

- Miri, A., Daie, K., Burdine, R.D., Aksay, E., and Tank, D.W. (2011). Regression-based identification of behavior-encoding neurons during large-scale optical imaging of neural activity at cellular resolution. *J. Neurophysiol.* 105, 964–980.
- Muto, A., Lal, P., Ailani, D., Abe, G., Itoh, M., and Kawakami, K. (2017). Activation of the hypothalamic feeding centre upon visual prey detection. *Nat. Commun.* 8, 15029.
- Nassi, J.J., and Callaway, E.M. (2009). Parallel processing strategies of the primate visual system. *Nat. Rev. Neurosci.* 10, 360–372.
- Naumann, E.A., Fitzgerald, J.E., Dunn, T.W., Rihel, J., Sompolinsky, H., and Engert, F. (2016). From Whole-Brain Data to Functional Circuit Models: The Zebrafish Optomotor Response. *Cell* 167, 947–960.e20.
- Niell, C.M., and Smith, S.J. (2005). Functional imaging reveals rapid development of visual response properties in the zebrafish tectum. *Neuron* 45, 941–951.
- Orger, M.B., Kampff, A.R., Severi, K.E., Bollmann, J.H., and Engert, F. (2008). Control of visually guided behavior by distinct populations of spinal projection neurons. *Nat. Neurosci.* 11, 327–333.
- Pologruto, T.A., Yasuda, R., and Svoboda, K. (2004). Monitoring neural activity and [Ca<sub>2+</sub>] with genetically encoded Ca<sub>2+</sub> indicators. *J. Neurosci.* 24, 9572–9579.
- Portugues, R., and Engert, F. (2009). The neural basis of visual behaviors in the larval zebrafish. *Curr. Opin. Neurobiol.* 19, 644–647.
- Presson, J., Fernald, R.D., and Max, M. (1985). The organization of retinal projections to the diencephalon and pretectum in the cichlid fish, *Haplochromis burtoni*. *J. Comp. Neurol.* 235, 360–374.
- Preuss, S.J., Trivedi, C.A., vom Berg-Maurer, C.M., Ryu, S., and Bollmann, J.H. (2014). Classification of object size in retinotectal microcircuits. *Curr. Biol.* 24, 2376–2385.
- Ramdy, P., and Engert, F. (2008). Emergence of binocular functional properties in a monocular neural circuit. *Nat. Neurosci.* 11, 1083–1090.
- Randlett, O., Wee, C.L., Naumann, E.A., Nnaemeka, O., Schoppik, D., Fitzgerald, J.E., Portugues, R., Lacoste, A.M., Riegler, C., Engert, F., and Schier, A.F. (2015). Whole-brain activity mapping onto a zebrafish brain atlas. *Nat. Methods* 12, 1039–1046.
- Recher, G., Jouralet, J., Brombin, A., Heuzé, A., Mugnieri, E., Hermel, J.M., Desnoulez, S., Savy, T., Herbomel, P., Bourrat, F., et al. (2013). Zebrafish midbrain slow-amplifying progenitors exhibit high levels of transcripts for nucleotide and ribosome biogenesis. *Development* 140, 4860–4869.
- Reinig, S., Driever, W., and Arrenberg, A.B. (2017). The Descending Diencephalic Dopamine System Is Tuned to Sensory Stimuli. *Curr. Biol.* 27, 318–333.
- Reiser, M.B., and Dickinson, M.H. (2008). A modular display system for insect behavioral neuroscience. *J. Neurosci. Methods* 167, 127–139.
- Rinner, O., Rick, J.M., and Neuhauss, S.C. (2005). Contrast sensitivity, spatial and temporal tuning of the larval zebrafish optokinetic response. *Invest. Ophthalmol. Vis. Sci.* 46, 137–142.
- Robles, E., Laurell, E., and Baier, H. (2014). The retinal projectome reveals brain-area-specific visual representations generated by ganglion cell diversity. *Curr. Biol.* 24, 2085–2096.
- Romano, S.A., Pietri, T., Pérez-Schuster, V., Jouary, A., Haudrechy, M., and Sumbre, G. (2015). Spontaneous neuronal network dynamics reveal circuit's functional adaptations for behavior. *Neuron* 85, 1070–1085.
- Ronneberger, O., Liu, K., Rath, M., Rueß, D., Mueller, T., Skibbe, H., Drayer, B., Schmidt, T., Filippi, A., Nitschke, R., et al. (2012). ViBE-Z: a framework for 3D virtual colocalization analysis in zebrafish larval brains. *Nat. Methods* 9, 735–742.
- Rupp, B., Wullimann, M.F., and Reichert, H. (1996). The zebrafish brain: a neuroanatomical comparison with the goldfish. *Anat. Embryol. (Berl.)* 194, 187–203.
- Sajovic, P., and Levinthal, C. (1982). Visual cells of zebrafish optic tectum: mapping with small spots. *Neuroscience* 7, 2407–2426.
- Schmitt, E.A., and Dowling, J.E. (1999). Early retinal development in the zebrafish, *Danio rerio*: light and electron microscopic analyses. *J. Comp. Neurol.* 404, 515–536.
- Schwartz, E.L. (1980). Computational anatomy and functional architecture of striate cortex: a spatial mapping approach to perceptual coding. *Vision Res.* 20, 645–669.
- Semmelhack, J.L., Donovan, J.C., Thiele, T.R., Kuehn, E., Laurell, E., and Baier, H. (2014). A dedicated visual pathway for prey detection in larval zebrafish. *eLife* 9, 3.
- Severi, K.E., Portogues, R., Marques, J.C., O'Malley, D.M., Orger, M.B., and Engert, F. (2014). Neural control and modulation of swimming speed in the larval zebrafish. *Neuron* 83, 692–707.
- Simpson, J.I. (1984). The accessory optic system. *Annu. Rev. Neurosci.* 7, 13–41.
- Spillmann, L. (2014). Receptive fields of visual neurons: the early years. *Perception* 43, 1145–1176.
- Tay, T.L., Ronneberger, O., Ryu, S., Nitschke, R., and Driever, W. (2011). Comprehensive catecholaminergic projectome analysis reveals single-neuron integration of zebrafish ascending and descending dopaminergic systems. *Nat. Commun.* 2, 171.
- Thiele, T.R., Donovan, J.C., and Baier, H. (2014). Descending control of swim posture by a midbrain nucleus in zebrafish. *Neuron* 83, 679–691.
- Trowe, T., Klostermann, S., Baier, H., Granato, M., Crawford, A.D., Grunewald, B., Hoffmann, H., Karlstrom, R.O., Meyer, S.U., Müller, B., et al. (1996). Mutations disrupting the ordering and topographic mapping of axons in the retinotectal projection of the zebrafish, *Danio rerio*. *Development* 123, 439–450.
- Walley, R.E. (1967). Receptive fields in the accessory optic system of the rabbit. *Exp. Neurol.* 17, 27–43.
- Wang, K., Hinz, J., Haikala, V., Reiff, D.F., and Arrenberg, A.B. (2019). Selective processing of all rotational and translational optic flow directions in the zebrafish pretectum and tectum. *BMC Biol.* 17, 29.
- Yamamoto, K., and Vernier, P. (2011). The evolution of dopamine systems in chordates. *Front. Neuroanat.* 5, 21.
- Yáñez, J., Suárez, T., Quelle, A., Folgueira, M., and Anadón, R. (2018). Neural connections of the pretectum in zebrafish (*Danio rerio*). *J. Comp. Neurol.* 526, 1017–1040.
- Zhang, M., Liu, Y., Wang, S.Z., Zhong, W., Liu, B.H., and Tao, H.W. (2011). Functional elimination of excitatory feedforward inputs underlies developmental refinement of visual receptive fields in zebrafish. *J. Neurosci.* 31, 5460–5469.
- Zimmermann, M.J.Y., Nevala, N.E., Yoshimatsu, T., Osorio, D., Nilsson, D.E., Berens, P., and Baden, T. (2018). Zebrafish Differentially Process Color across Visual Space to Match Natural Scenes. *Curr. Biol.* 28, 2018–2032.e5.

**STAR★METHODS****KEY RESOURCES TABLE**

REAGENT or RESOURCE	SOURCE	IDENTIFIER
Chemicals, Peptides, and Recombinant Proteins		
$\alpha$ -bungarotoxin	Sigma-Aldrich	T0195-.5MG
Poly-L-lysine solution	Sigma-Aldrich	P4832-50ML
Experimental Models: Organisms/Strains		
Zebrafish <i>Tg(HuC:GCaMP5G)a4598Tg</i>	Ahrens et al., 2013b	N/A
Zebrafish <i>Tg(th-E2A-QF2)m1512 x Tg(QUAS: EGFP)</i>	Driever lab (Freiburg University)	N/A
Software and Algorithms		
ImageJ/Fiji	NIH	<a href="https://fiji.sc">https://fiji.sc</a>
MATLAB R2010b, R2014b, R2015b	MathWorks	<a href="https://www.mathworks.com/products/matlab.html">https://www.mathworks.com/products/matlab.html</a>
LabVIEW 2015	National Instruments	<a href="http://www.ni.com/en-us/shop/labview.html">http://www.ni.com/en-us/shop/labview.html</a>
Mscan	Sutter Instrument	<a href="https://www.sutter.com/MICROSCOPES/mcs.html">https://www.sutter.com/MICROSCOPES/mcs.html</a>
Other		
Z-Brain Atlas	Randlett et al., 2015	<a href="https://engertlab.fas.harvard.edu/Z-Brain/">https://engertlab.fas.harvard.edu/Z-Brain/</a>

**LEAD CONTACT AND MATERIALS AVAILABILITY**

Further information and requests for resources and reagents should be directed to and will be fulfilled by the Lead Contact Aristides Arrenberg ([aristides.arrenberg@uni-tuebingen.de](mailto:aristides.arrenberg@uni-tuebingen.de)).

**EXPERIMENTAL MODEL AND SUBJECT DETAILS****Animal care and transgenic lines**

All animal procedures conformed to the institutional guidelines of the Universities of Tübingen and Freiburg and the local government (Regierungspräsidium Tübingen and Regierungspräsidium Freiburg, respectively). The transgenic zebrafish lines *Tg(HuC: GCaMP5G)a4598Tg* and the unpublished double transgenic line *Tg(th-E2A-QF2)m1512 x Tg(QUAS: EGFP)* (Fernandes et al., 2012; Reinig et al., 2017) were used in this study. Transgenic lines were kept in either a TL or TLN (nacre) background. Zebrafish larvae were raised in E3 medium until day 5 or 6 post-fertilization (dpf).

**METHOD DETAILS****Animal preparation (tectal and pretectal imaging of neuronal somata)**

At the day of experiments (5 or 6 dpf), larvae were transferred into a Petri dish and embedded in low melting agarose (E3 medium). The agarose surrounding the eyes was not removed as to minimize the range of possible eye movements. 6 animals received an injection of  $\alpha$ -bungarotoxin into the caudal vein to paralyze them and prevent eye movements and motion artifacts. 4 animals were recorded without paralysis. In addition, 6 animals were recorded without paralysis in another independent experiment and exclusively used for the analyses presented in the Figures S1B, S1C, S4B, and S4F. The animals were then transferred and mounted in agarose on a glass triangle and the fish head protruded the point of the glass triangle, so that the eyes could see through the (agarose and) water clearly. The agarose surrounding the fish head was trimmed on the sides and in front of the animal to reduce the amount of surrounding agarose (Figure S1F). However, the eyes were still covered by agarose to minimize the range of possible eye movements. The glass triangle was held from the back by a 5 mm thin shaft which was fixed to an 8 cm diameter glass bulb (made by a glass blower) filled with E3 medium. The glass bulb resembled a consumer market light bulb (threading of the light bulb/glass bulb shaft at the back of the fish) and a 5 cm diameter hole was cut on the top of the spherical part to allow for approach of the microscope objective onto the fish (Figure S1F). From stimulus arena to the fish eye, the light traveled through air, glass (light hit glass roughly orthogonally in the spherical part as to minimize refraction of light rays), water, and finally agarose. The glass bulb was fixed with its shaft (15.5 mm diameter) to the metal holder which allowed for pitch and yaw adjustments (the glass shaft allowed for adjustments in roll). In the first batches of receptive field mapping (n = 6 larvae) experiments, we noticed a problem regarding reflections on the glass bulb on the opposite side

of stimulation, resulting in detected neurons on the ipsilateral side of (intended) stimulation in the tectum (which were not plotted in Figure 3). In the second set of recordings (4 larvae), we wrapped a piece of black, half-cylindrical aluminum foil around the objective. The black aluminum foil was then lowered beyond the eye contralateral to the stimulus to prevent this eye from seeing the reflections. In these recordings, only very few ipsilateral tectal neurons were detected (and were not excluded in the anatomical registration figures). Both sets of recordings were included in data analysis, because only few additional neurons were detected due to the reflections in the ipsilateral tectum, suggesting that the vast majority of the detected neurons of the contralateral side were detected due to the stimulus presented to the intended eye.

### 2-photon microscopy of somatic calcium responses

Calcium imaging was performed with a two-photon microscopy setup based on the MOM microscope (Sutter Instruments; Euler et al., 2009), using a Coherent Vision-S Ti-Sa laser and a 20x/1.0 Zeiss objective to image calcium signals in the transgenic fish line HuC:GCaMP5G (*Tg(elavl3:GCaMP5G)a4598*) (Ahrens et al., 2013b). Calcium time series were recorded at 2 frames per second, with an image size of 512 × 512 pixels and 2 × magnifications, at 920 nm, pre-pulse compensation set to 9756 fs<sup>2</sup>. The midbrain and diencephalon were sampled from +60 μm below the landmark (posterior commissure) to –80 μm above the landmark. Optical slices were taken every 20 μm in the dorso-ventral direction in individual fish and across individual fish, and all dorso-ventral positions were recorded in 10 μm increments relative to the landmark (i.e., no recording at e.g., 5 or 15 μm below the landmark). Since we only recorded every 10 μm in dorso-ventral extent, more than twice as many neurons should have been detectable in the respective brain areas, had we sampled the brain areas at optimal spacing given the neuron soma diameter of ca. 5 μm. Where specified, error bars correspond to measures per completely imaged brain volume. Care was taken to record the same number of slices in each anatomical region. Two animals were used to image one complete brain volume (at 10 μm spacing). Due to the long recording times and positioning instability (likely resulting from the fish drifting within its agarose embedding), we corrected position drifts along the optical axis manually during the recording (mostly less than 4 μm per 30 minutes). Using the 20x objective and a magnification of 2x, our spatial resolution was 0.43 μm/pixel on the x axis (medial-lateral) and the y axis (anterior-posterior).

### LED arena for visual stimulation (Figures 1, 2, 3, and 4)

Visual stimulation of zebrafish was conducted with a cylindrical LED arena consisting of 14336 LEDs (Kingbright TA08-81CGKWA): 2 (arena halves) × 8 (rows) × 14 (columns) × 64 (8x8 multiplexed LED matrix) LEDs. The caudal-most column of each arena half was removed without LEDs (i.e., 14, not 15 columns), since the space was needed for the glass bulb stage metal holder. Therefore, the caudal-most stimulus patches were slightly cropped (18° azimuth instead of 30° azimuth for the last patch). The arena covered –168° to +168° in azimuth and –40° to 40° in elevation. A few degrees in angle of the dorsal field of view were likely blocked by the objective due to its access angle of 38.39° (< 40°), however the eyes were located ~200 μm below the objective focus which should have resulted in a maximal viewing angle exceeding 38.39° (i.e., 39.2°). The LEDs emitted at 570 nm and an additional high-pass filter foil (LEE no. 779, article 595-1700-7790, castinfo.de, Hagen, Germany) and diffusion filter foil (LEE no. 252, article 595-1780-2520) were placed in front of the arena to optimize GCaMP signal detection and make the stimulus appear more homogeneous. This resulted in a yellow appearance of the stimulus. The LED arena was controlled as described previously (Joesch et al., 2008; Reiser and Dickinson, 2008). LEDs lit during fly-back time of the scanning mirrors.

### Identification of regions of interest (imaging of neuronal somata)

For analysis of neuronal activity, a custom MATLAB script (MOM Load) identified regions based on their correlation to the stimulus and ROIs were manually drawn as described previously (Kubo et al., 2014; Miri et al., 2011). The 3-dimensional mapping of cell location was performed using custom written MATLAB scripts (Midbrain\_Localizer and Cell\_Viewer), which allowed to register the 2 dimensional recordings to a 3D z stack which was acquired after recording sessions (Kubo et al., 2014). See Figure S4 from Kubo et al. (2014) for an illustration of the 3-dimensional mapping procedure.

### Defining the borders of the tectum in our 3D datasets

To distinguish pretectal from tectal neurons, we proceeded as follows: For each fish, the whole z stack – which was imaged from the top of tectum to deep ventral pretectum and dorsal thalamus – was resliced to generate a transverse view. On selected, regularly spaced transverse planes (more than ~50 planes), the ventral border of the tectum was drawn: on each of these transverse plane (512 pixels from left to right, x dimension), a curve was drawn through the area devoid of neuronal somata or fluorescence that was ventrally adjacent to periventricular tectal area with densely packed, fluorescent somata. From each curve, 51 homogeneously distributed points were selected as key points with which a new boundary curve was generated by linear interpolation or three-term Gaussian fitting. Using this method, we obtained a boundary curve with 512 data points corresponding to the pixels in x/y dimensions (left-right and dorsal-ventral) for each transverse plane. In-between the annotated transverse planes, the 2D curves were interpolated to receive a surface that separated the tectum from the pretectum in all three dimensions (Wang et al., 2019). However, the boundaries between the caudal pretectum and adjacent brain areas in the posterior side (tegmentum) were not clearly visible in the GCaMP5G fish line. Referring to the AMC structure reported before (Kubo et al., 2014), and to the anatomical annotations of the

caudally adjacent tegmentum (Ronneberger et al., 2012; Randlett et al., 2015), the neurons below the tectal-pretectal boundary drawn above, which were located more than 140  $\mu\text{m}$  caudally to the posterior commissum, were excluded from the pretectum in the current study.

#### Registration of 3D pretectal volume from Z Brain atlas (related to Figure S6)

The pretectal region mask, obtained from datasets MaskDatabase.mat and Ref20131120pt14pl2.nrrd (Z Brain atlas, <https://engertlab.fas.harvard.edu/Z-Brain/download>) was used as the standard brain corresponding to the pretectal region mask.

- (1) The brain regions corresponding to our recordings (mainly tectum and dorsal diencephalon) were cropped out from the standard brain (size 282  $\times$  282, pixel  $\times$  pixel; 1 pixel = 0.798  $\mu\text{m}$ ). The cropped image was resized to 512  $\times$  512 (1 pixel = 0.43  $\mu\text{m}$ ) to match our image size and scale.
- (2) The standard coordinate system which we use in our zebrafish brain was drawn in the standard brain of the Z Brain atlas (Figure S4 from Kubo et al., 2014). The relative locations of the pretectal region boundary to the point of origin (0, 0, 0) were calculated.
- (3) The angle of the pretectal neuropil from the standard brain of the Z Brain atlas was measured with ImageJ. Compared to the standard pretectal neuropil angle of our own recordings (17.4°), the corresponding angle of the standard brain from the Z Brain atlas is pitched up, with a pretectal neuropil angle of 36.5°. Therefore, the pretectal region mask was rotated to register with our standard fish brain.
- (4) The pretectal volume was plotted with MATLAB with the rotated data.

#### Movies of 3D brain volumes with neurons shown inside

The cell locations (e.g., the colored balls in Figure 2A) were registered to the 3D matrix which corresponds to a z stack of one larval brain, with the intersection point of the first two landmark lines as coordinate origin (0, 0, 0). In the 3D matrix, 3D spheres representing the neurons were plotted and the new 3D matrix was saved as an image series. Then the new image series and the standard zebrafish brain image series were merged with ImageJ. 3D brain volumes with neurons highlighted in different colors were generated with ‘3D Viewer’ in ImageJ.

#### Monocular receptive field mapping

In the monocular receptive field mapping experiments, we used horizontally moving gratings, 0.033 cycles/ $^{\circ}$ , moving at 30°/s, as visual stimuli to induce the neural activities. 8 fish were recorded using naso-temporal motion, and 2 fish were recorded using temporal-nasal motion. The data was pooled because we didn't observe obvious difference in RF characteristics (RF size, RF centers). The additional recordings for Figures S1B, S4B, and S4F were performed using both naso-temporal and temporal-nasal motion for 6 fish (3 temporal-nasal and 3 naso-temporal, respectively). Three repetitions of the 57 stimulus phases were shown to the right eye of the fish using one half-cylindrical arena (Figure 1A). All the stimulus patterns were presented in the order depicted in Figure S1A. In each trial, every 4.8 s stimulus phase was preceded by a 4 s pause and followed by a 2 s pause with the same stationary visual stimulus pattern. At the beginning and the end of each repetition, we inserted 9 s pauses.

RF maps for individual neurons were calculated by a series of analysis steps. First, we filter the DFF fluorescence traces with a low pass wavelet decomposition [type Daubechies, MATLAB: wavedec(DFF, 1, 'db4')] and a sliding median filter (the median of three data points). Then deconvolution was performed to the filtered data with the decay time constant ( $\tau$ ) of GCaMP5G, 1.5 s. We calculated the mean of phase-averaged signal (MPAS, averaged over stimulus phase time) from the deconvolved traces. The baseline was defined as the MPAS of all the non-stimulus phases (i.e., without moving stimulus). The standard deviation (STD) of all phase-averaged signals was calculated for the non-motion phases. And the z-score was calculated using the equation:

$$z\text{-score} = (\text{MPAS} - \text{mean}(\text{baseline})) / \text{STD}(\text{baseline})$$

We then calculated the median MPAS z-score (i.e., the median across the three repetitions of a stimulus phase of the average of all data points within one stimulus phase).

To determine the size of receptive fields (RFs) of individual cells, we defined 5 subclasses of responses: small-size receptive fields, medium-size receptive fields, large-size receptive fields, bar-shaped receptive fields and double-field receptive fields (containing two discrete excitatory patches in the visual field). Since our stimulation protocol didn't allow for precise mapping of receptive fields (also Gaussian fits for larger receptive fields were problematic), we turned to a broad classification of RF sizes. To this end we used the smallest stimulation field (30° in azimuth, 13° in elevation) as a calculation unit (i.e., 1 “patch”). After manual inspection of the receptive field locations, we arbitrarily set the thresholds for the 3 size categories as 3 or less active phases (small, SM), 7 or less active phases (medium, ME) and 8 or more active phases (large, L). Bar cells were classified as having active phases only in the full vertical or full horizontal axis, while “double fields” were classified if they had two peaks of activation that were at least 60° away from each other. Most double-field receptive fields likely resulted from experimental

artifacts, in which stimulus reflections can cause such double field RFs. Neurons with double-field RFs were therefore excluded from further analysis.

To classify cells according to their respective size criteria, we ran a 2-step process:

**Step I**

1. Calculate mean patch density (MPD)
  - a. If the cell responded maximally during the small 6x6 stimulus phases, the MPD corresponded to the average normalized activity of the cell in the phases of the 6x6 stimuli.
  - b. If the cell responded maximally for one of the larger stimulus phases, the MPD was calculated as the average normalized activity of the cell in the phases of the 6x6 stimuli that were covered by the field of maximum activation (e.g., the cell in [Figure 1](#)Div had its maximal activity during in the upper horizontal bar stimulus phase, so the mean patch density would correspond to the average activity of the 6 upper patches of the 6x6 stimulation phase).
2. Next, we set the threshold for classifying a part of the visual field as “active” as follows: **IF**
  - a. MPD is smaller than 30%:
    - i. MPD \* 3
  - b. MPD is larger than 30% and smaller than 40%:
    - i. MPD \* 2
  - c. MPD is larger than 40%:
    - i. 90%

By relating the activity during the small stimuli to the activity observed during the larger stimuli, these MPD thresholds helped to obtain a more accurate quantification of active patches of cells preferentially active during the small stimulation phases.

3. In **Step I**, cells were classified if following criteria were met:
  - a. The maximum activity in the 6x6 stimulation phase exceeded Mean patch density \* factor (see step I.2) **or**
  - b. Maximum excitation in the 6x6 stimulation phase larger than 90%
4. To classify the number of active patches, we applied the threshold defined in **point I.2**

Cells were then either classified as ME or SM based on the number of active patches.

All cells that didn't meet the criteria from point I.3 were classified according to **Step II**. First, we calculated a second metric, the mean excitatory density (MED). We calculated the MED by multiplying the calcium response magnitude for each motion phase (excluding the 36 smallest motion phases) with an area factor (full size x 1, half size x 2 ...), resulting in a motion phase's calcium activity weighted by the visual field area in which the stimulus was moving. We call this parameter the “excitatory density” of the stimulated part of the visual field. A biologically plausible underlying cause for differences in excitatory density is the number of DS RGC inputs the cell receives from the portion of the visual field in which the stimulus moves. We then summed the excitatory densities from all larger stimulation fields together (1x1, 2x1, 1x2, 2x2, 1x6, 6x1) taking into account their spatial location in the visual field. This resulted in an excitatory density map of the complete visual field covered by the stimulus arena. In order to report a single number for the RF size, we then defined active phases as those having 75% or more of the normalized summed maximum activation. The difference between this threshold and the 90% threshold for SM cells is derived from comparing manual and automated classification methods.

This method favors smaller receptive fields, because the calcium indicator only shows disproportionately small fluorescence levels for low levels of calcium activity - i.e., it is non-linear - but it enables easy classification of cells size preferences with the given limitations of the calcium indicator ([Chen et al., 2013; Pologruto et al., 2004](#)).

The results from our analysis, which is based on thresholding and classification, fits well with both the results obtained from an automated approach using PCA and clustering ([Figure S2](#)), and results from manual classification of receptive field sizes.

To determine if cells were small-size selective, we compared the responses to small-size and larger-size stimuli from our stimulus protocol. If (i) a cell was assigned to the small size (SM) or median size (ME) category and was identified during one of the 36 (6x6) small-size stimulation phases (see above), and (ii) the cell showed its maximum activity during the 6x6 stimulation then this cell was classified as being size selective ('Inhibition').

To determine the relative reduction in activity (relative to the response if only the small excitatory receptive field is stimulated) and to visualize the spatial structure of the inhibitory receptive field (“inhibitory density”), we summed the relative reduction of activity (analogous to the above described excitatory density) for every patch belonging to the RF and removed the patches that were part of the RF from the inhibitory field.

Please note that some cells were assigned SM or ME status based on the excitatory density map (and not based on the 36 small-size stimulation phases). We assigned the “no inhibition” status to all of these cells, because the maximal activity was not found in any of the small-size stimulation phases. However, the RFs of these cells could still show some form of inhibition (e.g., during presentation of larger half-field stimulus phases), which was not characterized here. The second cell in [Figure 1](#)Dii (an ME cell) is an example for such cells without assigned “inhibition” status.

We estimated the RF centers in XY space as the center of mass of the normalized activity in the active phases (those with red dots in [Figure 1D](#)), i.e., both location and level of activity in active phases determined the position.

The median receptive field size across the visual field was derived by calculating (for every visual field position) the median RF size of receptive fields that covered the respective visual field location to visualize the distribution of RF sizes in the visual space.

LED arena light rays that traveled roughly through the center of the glass bulb (where the fish head was located as well) hit the glass bulb wall on the opposite side with an angle of incidence of 90°. This resulted in about 4% of reflected light (according to the Fresnel equations) and this light was visible to fish eye that was not intended to be stimulated. In the first 6 animals, we noticed an unexpectedly high number of detected ROIs in the optic tectum ipsilateral to the stimulation. The vast majority of these tectal ipsilateral ROIs had a reversed retino-tectal topography indicating that these ROIs were detected because of the reflected light. We decided to exclude these ROIs in the anatomical reconstruction. For the other 4 animals, we blocked the non-stimulated eye by placing a half-cylindrical piece of black aluminum foil around the objective and lowering it below the level of the eye. In these animals, a much smaller number of neurons were detected in the ipsilateral tectum, and their anatomical location corresponded to the expected retino-tectal topography. In the data analysis, the small-size RF neurons in the ipsilateral hemisphere recorded from the first 6 animals were excluded. The laterality index for tectal neurons was -0.88 for the 4 animals with one blocked eye, and -0.46 for the 6 animals in which the eyes were not blocked.

In [Figure 3A](#) (locations of RF centers in the visual field for tectal small-size RF cells), only very few cells (55 out of 1074), which have RFs centers in the lower temporal of the visual field, were present. While we are convinced that this finding represents an actual under-representation of such cells in the optic tectum, we would like to discuss two experimental caveats, which can explain the effect partially (but not fully). First, the fish were mounted on a glass triangle and care was taken to allow free view of the stimuli from the position of the eye lenses by pushing the larva toward the tip of the glass triangle (thereby reducing the positional stability of the recording). However, for some animals, a small portion of the lower temporal visual field might have been blocked by the sides of the glass triangle. However, this caveat should only have affected extreme lower-temporal receptive field positions (e.g., > 120° in azimuth and < -30° in elevation). Second, the anatomical positions of those tectal neurons having lower temporal receptive field centers lie close to the border with the pretectum. The pretectum-classified small-size RF cells in proximity of the tectum (shade red dots in [Figure 2A](#)) can fill the gap in the ventral-caudal visual field in [Figure 3A](#) only partially (just 12 additional cells for the region > 90° azimuth and < 0° elevation) when such pretectal neurons are plotted together with the tectal neurons.

To characterize the distributions of RF centers across visual space, the density of the RF centers in the visual space was calculated with 'ksdensity' function in MATLAB. Contour lines were plotted based on the density.

One gap between the rostral diencephalic and caudal pretectal neurons is quite obvious ([Figure 2A](#)). Moreover, in the rostral diencephalon, many neurons are small-size selective (RFs with signs of inhibition). Therefore, a boundary was manually defined between the rostral diencephalon and caudal pretectum along this gap containing only few motion-sensitive neurons ([Figure 2A](#)). In the data analysis of the rostral diencephalic neurons, the rostral diencephalon was defined as follows: dorso-ventral axis < 10 μm and anterior-posterior axis < 60 μm, or dorso-ventral axis < -30 μm and anterior-posterior axis < 110 μm. 140 μm caudal to the posterior commissure along the anterior-posterior axis was conceded as the caudal boundary of the pretectum with other brain areas. The bilaterally symmetric anatomical distribution of the neurons relative to the midline was measured using a laterality index, which was calculated as,

$$(neurons_{right} - neurons_{left}) / (neurons_{left} + neurons_{right}).$$

### Inclusion criteria for somatic calcium responses

We calculated the Pearson's linear correlation coefficients between the stimulus phase z-scores (see above) of the three stimulus protocol repetitions (for all 3 pairwise combinations) to characterize the reproducibility of stimulus-evoked calcium responses. In our further data analysis, we only kept the neurons for which all three correlation coefficients were higher than a certain threshold. The threshold was set between 0.65 and 0.75 to exclude around 30% neurons with low reproducibility of stimulus-evoked activity in the monocular receptive field mapping experiment (2004 out of 2995, 67% neurons were kept). We then performed signal-to-noise ratio (SNR) analysis to exclude neurons with unstable baseline. In the SNR analysis, a threshold of four was used on the z-score to detect positive neural responses. SNR was defined as the ratio of the average response of all the responsive phases to the standard deviation of the baseline. All neurons with SNR lower than a certain threshold were excluded. The threshold was set between 8 and 10 to exclude about 5% remaining neurons with low SNR. We kept about 96% (1926 out of 2004 neurons) in the monocular receptive field mapping experiment for further analysis.

### Setup for measuring the receptive field of OMR behavior

The visual stimuli were presented binocularly with a 336° (from -168° to 168° in azimuth) surround LED arena (two half-cylindrical arenas, [Figure 4A](#)) from both sides of the fish, i.e., all stimulus phases (except the rotational and looming control stimuli) were mirror-symmetric across the midline. The image of the fish was reflected to a lens by a mirror positioned around 5 cm above the fish (1 cm above the glass bulb). An infrared-sensitive high speed camera (Model IDT iNDustrial Speed I, Integrated Design Tools Inc.) with an IR bandpass filter (ET 850/40, CHROMA) recorded (250 Hz) the behaviors of the fish through the lens (diameter,

25.4 mm; focal length, 100mm; THORLABS, LB1676) mentioned above. Since the mirror above the fish is tilted 45 degrees vertically, the light path from the mirror to the camera was horizontal. The fish was illuminated from below with a high power infrared LED light (850 nm, Conrad, Item No. 491248-62) positioned 1 cm below the glass bulb. The infrared light was mounted below a piece of milk glass and provided homogeneous background illumination around the fish (Figure S5A). The infrared LED light and the camera were triggered by the motion signal of the visual stimulus recorded by a LabVIEW DAQ box. In our experiment, the camera started recording about 300 ms after the motion phase onset of the visual stimuli. The infrared LED light was only on during the motion visual stimulus phases to reduce potential harm to the fish.

### Receptive field mapping of OMR behavior

For each recording, a larval zebrafish (6 dpf) was transferred into a Petri dish and embedded in low melting agarose (E3 medium) on a glass triangle such that the fish body completely protruded the tip of the glass triangle. The agarose surrounding the larval tail was removed to free the tail. To reduce the amount of agarose surrounding the animal, agarose surrounding the fish was trimmed on the sides and in front. Only the agarose caudal to the animal attached to the triangular stage. Therefore, a large view field was accessible for the fish, and - more importantly - the contours of the beating tail could be imaged without optical obstruction from the glass triangle. The fish and the glass triangle were fixed to an 8 cm diameter glass bulb filled with E3 medium in the same way as described above (see *Animal Preparation* in the *Method Details* section). The animal was illuminated from below with a high power infrared LED light, which was triggered on 150 ms after the start of the grating motion and lasted for 10 s. During the first 6 s of each grating motion phase (300 ms delay), the animal was imaged with a high speed infrared camera at 250 frames per second. The video data were saved during the pauses and analyzed with custom written MATLAB code offline.

In the OMR behavioral test, forward moving gratings, 0.033 cycles/ $^{\circ}$ , moving at 30 $^{\circ}$ /s, were used as visual stimuli to induce the optomotor response. Three repetitions of the 55 stimulus phases were shown to both eyes of the fish using two half-cylindrical arenas. All stimulus patterns were presented in each of the three randomized orders depicted in Figure S5C for the repetitions. The animals were adapted to the stationary gratings for about half an hour before motion stimulation started. In each trial, every 9.75 s stimulus phase was preceded by an 18 s pause and followed by a 51 s pause with the same stationary visual stimulus pattern. Before presenting the 2<sup>nd</sup> and 3<sup>rd</sup> repetition of the 55 stimulus phases, the animals rested for about 1 hour.

The motion of the larval tail was traced using a custom MATLAB algorithm for image processing and the 'alpha angle' (the angle between the fish anterior-posterior body axis and the tail tip, see Figure 4A) was calculated. The single tail beats were detected by labeling the peaks and troughs of the alpha angle traces. In our analysis, only swim beats meeting the following two criteria were considered as forward OMR beats: (1) the tail-beat frequency (during individual swimming bouts) was higher than 25 Hz; (2) for each beat, the difference of the amplitudes of adjacent peaks and troughs divided by the sum of them was smaller than 0.3 and larger than -0.3 (symmetrical tail beats/forward swimming).

Two types of OMR tail beats were distinguished: symmetrical and unsymmetrical tail beats (Figures 4E and S5F). Unsymmetrical tail beats oftentimes occurred at the beginning and the end of OMR tail beat bouts (Figures 4E and S5F), similar to the case of freely swimming larval zebrafish (Marques et al., 2018). As expected, the larval zebrafish tried to turn in response to the rotating visual stimulus used as control in our protocol, with tails beating mainly unilaterally to the reverse direction of the rotation (Ahrens et al., 2013a). However, symmetrical tail beats were observed in the turning swimming bouts as well (Figure S5F).

In Figure 4 (and Figure S5), the shown tail-beat frequency does not correspond to the frequency reached during individual swim bouts, but instead corresponds to the average frequency during the stimulus phase, such that time periods without swim bouts lead to a reduction of tail-beat frequency.

### QUANTIFICATION AND STATISTICAL ANALYSIS

The statistical information calculated with MATLAB R2014b built-in functions is provided in each of the sections above. For statements of significance an alpha level of 0.05 was used unless stated otherwise.

The analyzed number of zebrafish and brains is indicated in the main text and figure legends. Error bars correspond to SEM unless stated otherwise.

### DATA AND CODE AVAILABILITY

The scripts for data pre-processing and the pre-processed data are freely available from our G-Node repository ([https://gin.g-node.org/Arrenberg\\_Lab/monocular\\_receptive\\_field\\_mapping](https://gin.g-node.org/Arrenberg_Lab/monocular_receptive_field_mapping)). The original raw datasets have not been deposited at G-Node due to the large data size. All raw and processed data and software used to generate the figures will be made available upon request.